Nanoscale

REVIEW

View Article Online
View Journal | View Issue

Cite this: *Nanoscale*, 2024, **16**, 9680

Enhanced photocatalytic performance of SnS_2 under visible light irradiation: strategies and future perspectives

Ardiansyah Taufik, *[a] Rosari Saleh [b,c] and Gimyeong Seong *[d]

Received 19th February 2024,
Accepted 16th April 2024

DOI: 10.1039/d4nr00706a

rsc.li/nanoscale

Tin(II) sulfide (SnS_2) has emerged as a promising candidate for visible light photocatalytic materials. As a member of the transition metal dichalcogenides (TMDs) family, SnS_2 features a band gap of approximately 2.20 eV and a layered structure, rendering it suitable for visible light activation with a high specific surface area. However, the application of SnS_2 as a visible light photocatalyst still requires improvement, particularly in addressing the high recombination of electrons and holes, as well as the poor selectivity inherent in its perfect crystal structure. Therefore, ongoing research focuses on strategies to enhance the photocatalytic performance of SnS_2. In this comprehensive review, we analyze recent advances and promising strategies for improving the photocatalytic performance of SnS_2. Various successful approaches have been reported, including controlling the reactive facets of SnS_2, inducing defects in the crystal structure, manipulating morphologies, depositing noble metals, and forming heterostructures. We provide a detailed understanding of these phenomena and the preparation techniques involved, as well as future considerations for exploring new science in SnS_2 photocatalysis and optimizing performance.

1 Introduction

The family of transition metal dichalcogenides (TMDs) has garnered significant attention in photocatalytic applications owing to its visible light band gap and layered structure, which provides a high specific surface area.[1,2] However, the traditional utilization of primary TMD materials such as MoS_2, $MoSe_2$ and WS_2 has predominantly been as supporting photocatalysts alongside other materials like ZnO,[3–6] TiO_2,[7–10] C_3N_4 [11] and others, due to their properties akin to graphene.[12,13] In contrast, unlike MoS_2, $MoSe_2$ and WS_2, SnS_2 has emerged as a promising photocatalyst under visible light irradiation, attributable to its suitable band gap energy for visible light.[14,15]

SnS_2 belongs to the family of layered structure transition metal dichalcogenides (TMDs), characterized as an n-type semiconductor with a band gap ranging from 2.18 to 2.44 eV.[16] In practical applications, SnS_2 has found widespread use across various fields such as batteries,[17,18] sensors,[19,20] and photocatalysis due to its low cost, low toxicity, excellent stability, and abundant natural reserves.[21] SnS_2 can be synthesized using various techniques, including hydrothermal,[22,23] solvothermal,[24,25] CVD,[26,27] and pulse laser deposition,[28–30] among others. Additionally, SnS_2 can exhibit diverse morphologies, such as flower-like structures, plate-like forms, nanoparticles, and quantum dots, rendering it particularly intriguing for both study and application purposes.

Various reports have shown that SnS_2 can be utilized in numerous photocatalytic applications, such as hydrogen production,[31–34] wastewater treatment,[35–39] antibacterial and antifungal activity,[40–43] and air purification.[44] For example, Yu *et al.*[45] first reported the photocatalytic hydrogen production of SnS_2 nanosheets under solar light simulation with H_2 evolution activity of 1.06 mmol h^{-1} g^{-1}. In the case of waste water remediation, there are numerous reports for different kinds of waste water such as heavy metals,[46–48] organic dyes,[49,50] and pharmaceutical waste.[51–53] For antibacterial activity, SnS_2 has been applied to inactivate *S. aureus* and *E. coli* as reported by Fakhri *et al.*,[40,41] and for air purification SnS_2 has been reported to be able to remove various VOC gasses such as trichloroethylene[54] and formaldehyde[55] as well as NO_x gas.[44] Other applications have also been reported by researchers such as CO_2 reduction and nitrogen fixation which make SnS_2 a promising photocatalyst candidate. (For detailed summaries see sub-section 2.2.)

[a]*WPI – Advanced Institute for Materials Research (WPI-AIMR), Tohoku University, 2-1-1 Katahira, Aoba-ku, Sendai, Miyagi 980-8577, Japan.*
E-mail: ardiansyah.taufik.d2@tohoku.ac.jp
[b]*Departement Fisika, FMIPA Universitas Indonesia, Kampus UI Depok, Depok 16424, Indonesia*
[c]*Integrated Laboratory of Energy and Environment FMIPA Universitas Indonesia, Kampus UI Depok, Depok 16424, Indonesia*
[d]*Department of Environmental and Energy Engineering, The University of Suwon, 17, Wauan-gil, Bongdam-eup, Hwaseong-si, Gyeonggi-do, 18323, Republic of Korea*

As a photocatalyst, some characteristics of SnS_2 have become key for an excellent performance. These include low recombination and hole rates,[56–59] a high specific surface area,[60,61] high-reactivity facets,[62,63] and good stability.[64,65] Despite the confirmed photocatalytic performance of SnS_2, there are still limitations that hinder its efficiency, such as a high recombination of electrons and holes,[66,67] and low specific surface area. Consequently, many researchers have focused on modifying SnS_2 to meet the requirements.

Several strategies have been widely adopted to enhance photocatalytic performance, including morphological modification,[68,69] structural engineering,[70,71] and heterostructure formation.[72–74] Each of these strategies has unique advantages. For instance, morphological modification can alter the surface structure of SnS_2, influencing parameters such as surface area and facet arrangement, which are beneficial for improving photocatalytic performance. Structural engineering involves disturbing the crystal structure of SnS_2 through various treatments, including vacancy generation, doping addition, and strain engineering. These treatments effectively decrease electron and hole recombination, thereby enhancing photocatalytic performance. Noble metal doping, such as Au, Pt, and Ag, is a well-known method for improving photocatalytic performance due to its ability to act as an electron acceptor, slowing down the recombination of electrons and holes.[75] Meanwhile, heterostructure formation can generate a synergistic effect between one sample and another, effectively improving the photocatalytic performance.[76]

Presently, there are several reports that have reviewed the photocatalytic performance of SnS_2. Sharma *et al.*[77] reviewed the photocatalytic performance of SnS_2 related to energy conversion and a heterostructure perspective approach, while Guo *et al.*[78] reviewed the advancement of the photocatalytic performance of SnS_2 by comparing pure SnS_2 and SnS_2-based composite. While these two reviews have addressed some important aspects of improvement strategies, the detailed explanation and fundamental mechanism of the photocatalytic enhancement of SnS_2 have not been thoroughly explored. In this study, we systematically investigate the current advancement strategies for enhancing photocatalytic performance, which can be classified into three categories: structural modification, morphology engineering, and heterojunction formation. We will elucidate the factors from each strategy that have the most significant impact on the photocatalysis of SnS_2. Furthermore, we will propose future perspectives for the development of photocatalytic studies on SnS_2 based on the existing literature. Fig. 1 illustrates three distinct strategies for enhancing photocatalytic performance across various applications, discussed in this review. The first strategy involves structural modification, encompassing vacancy generation and doping processes. The second strategy focuses on morphological manipulation, featuring a range of morphologies such as nanoflowers, nanoparticles, nanosheets, and quantum dots. The final strategy concerns heterojunction formation, encompassing Schottky junctions, heterojunctions types I and II, p–n junctions, as well as Z-scheme and S-scheme photocatalysts. Additionally, we address current challenges and offer insights into future developments.

2 SnS_2 properties and photocatalytic applications

2.1 Physical properties of SnS_2

Tin disulfide (SnS_2) belongs to the IV–VI chalcogenide materials and exhibits a golden-yellowish color, resembling the configuration of transition metal dichalcogenide (TMD) materials.[77] The atomic arrangement of SnS_2 consists of a Sn atom sandwiched between two hexagonally close-packed sulfur atoms. In layered SnS_2, planar threefold layers (TLs) are

Ardiansyah Taufik

Dr Ardiansyah Taufik earned his Ph.D. degree from the Graduate School of Environmental Studies, Tohoku University, in 2021. His research interests lie in the development of nanomaterials for environmental applications, including gas sensors and photocatalysts. From 2021 to 2024, he served as a Specially Appointed Assistant Professor at the New Industry Creation Hatchery Center (NICHe), Tohoku University. As of April 1st, 2024, he has transitioned to the role of Specially Appointed Assistant Professor at the Advanced Institute of Materials Research (AIMR) Tohoku University, focusing on research involving the flow-reactor hydrothermal synthesis of ultra-small nanoparticles.

Rosari Saleh

Dr Rosari Saleh, a full Professor at the Faculty of Mathematics and Natural Science, Universitas Indonesia, earned her B.Sc. in Physics from the same institution in 1985 and her Ph.D. in Physics from Philipps-Universität Marburg, Germany, in 1990. She joined Universitas Indonesia in 1994, and became a full Professor in 2007. Her research interest is in the application of metal oxide nanoparticles for photocatalytic applications. Until now, she is recognized for her prolific publication record in high-quality papers on photocatalytic research.

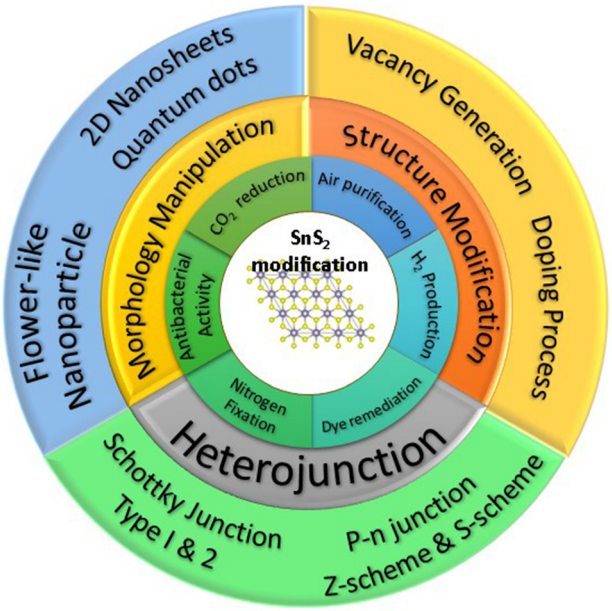

Fig. 1 Modification strategy of SnS_2 for improving photocatalytic performance.

formed, where strong covalent bonding exists in a plane, while weak van der Waals interactions dominate out of plane, as shown in Fig. 2(a).[79] The SnS_2 structure belongs to the covalent bonding group of $P\bar{3}m1$ (164) with lattice parameters $a = b =$ 0.3643 nm and $c = 1.7683$ nm.[79] Like the other members of the TMD family, SnS_2 has a layered structure with several interesting properties such as a high optical absorption coefficient, tunable bandgap, low toxicity, and natural abundance, which makes it very promising for 2D material applications such as photocatalysis, photoanodes,[80] and gas sensors.[20] SnS_2 corresponds to an n-type semiconductor that possesses a narrow energy band gap of 2.0–2.4 eV. The band positions of SnS_2 were determined by linear extrapolation of the band edges and secondary electron cut-off, to the baseline, and yielded an ionization potential ($E_{vac} - E_{VBM}$) of 6.44 ± 0.07 eV and an electron affinity ($E_{vac} - E_{CBM}$) of 4.16 ± 0.17 eV. A bandgap ($E_{CBM} - E_{VBM}$) of 2.28 ± 0.15 eV is thus found that corresponds to the indirect band gap as shown in Fig. 2(b). SnS_2 also has higher electron mobility (~230 $cm^2\ V^{-1}\ s^{-1}$), higher capacitance (645 mA h g^{-1}), and lower environmental noxiousness.[81] The photocatalytic reaction process occurs when the band positions of the photocatalyst align with the redox potentials required for specific chemical reactions. For instance, the conversion of H^+ to H_2 can occur at 0 V *vs.* NHE energy, where electrons in the conduction band with an energy lower than 0 V can reduce H^+ to H_2. Conversely, the transformation of OH^- to $OH^\bullet$ requires 1.93 V *vs.* NHE, necessitating holes with an energy higher than 1.93 *vs.* NHE to oxidize OH^- to $OH^\bullet$. In this context, the band positions of SnS_2 fulfill both criteria, with the conduction band at −1.5 V *vs.* NHE and the valence band at 2.13 V *vs.* NHE,[82] as illustrated in Fig. 2(c). Various chemical reactions may yield different potential energy requirements, thus influencing the applicability of SnS_2 in photocatalysis.

2.2 Photocatalytic applications of SnS_2

The utilization of SnS_2 as a photocatalyst was initially documented in 2007 by He *et al.*[83] who explored the formation of a heterostructure between SnS_2 and TiO_2 for methyl orange degradation. However, after this initial investigation, research on SnS_2 photocatalysis remained limited until 2017, when the number of publications on the subject notably increased, as illustrated in Fig. 3(a). Presently, the total number of publications on SnS_2 as a photocatalyst remains at less than 500, significantly lower compared with conventional photocatalysts such as TiO_2 or ZnO, and even other transition metal dichalcogenide (TMD) materials like MoS_2 and WS_2 (based on Scopus data). As a 2D photocatalyst material, SnS_2 has found applications across various domains, including air purification,[44,55] wastewater treatment,[47,84–87] hydrogen production,[88–97] and antibacterial purposes,[41] CO_2 reduction, and[89,91,98–100] nitrogen fixation.[92,94,101]

According to Scopus data, illustrated in Fig. 3(b), the predominant focus of photocatalytic applications involving SnS_2 is wastewater treatment, constituting 66% of the total research publications to date. Following closely, hydrogen production and CO_2 reduction make up 21% and 10% of the total publications on SnS_2 as a photocatalyst. The least explored applications include nitrogen fixation, antibacterial activity, and air purification. Wastewater treatment represents the most extensively studied application when investigating SnS_2 photocatalytic performance. Given the high demand for clean water in our daily lives, the removal of wastewater from water resources is of paramount importance. Various types of wastewater, containing pollutants such as organic dyes, heavy metals, pharmaceutical waste, and even uranium(VI), pose significant threats to our health. Until now (2024 January 10th), based on Scopus data there are 337 publications that have reported the use of SnS_2 photocatalyst for wastewater treat-

Gimyeong Seong

Dr Gimyeong Seong, an assistant professor at The University of Suwon, obtained his Ph.D. in Chemical Engineering, specializing in supercritical fluid technology, from Tohoku University, Japan, in 2012. Until March 2023, he contributed to collaborative research in Japan, focusing on nanomaterial synthesis and catalysis. As an associate professor at Tohoku University New Industry Creation Hatchery Center (NICHe), he fostered collaborations with researchers worldwide. Since April 2023, Dr Seong has focused on hydrogen energy and renewable energy systems at the University of Suwon, publishing numerous papers in international journals and passionately mentoring students.

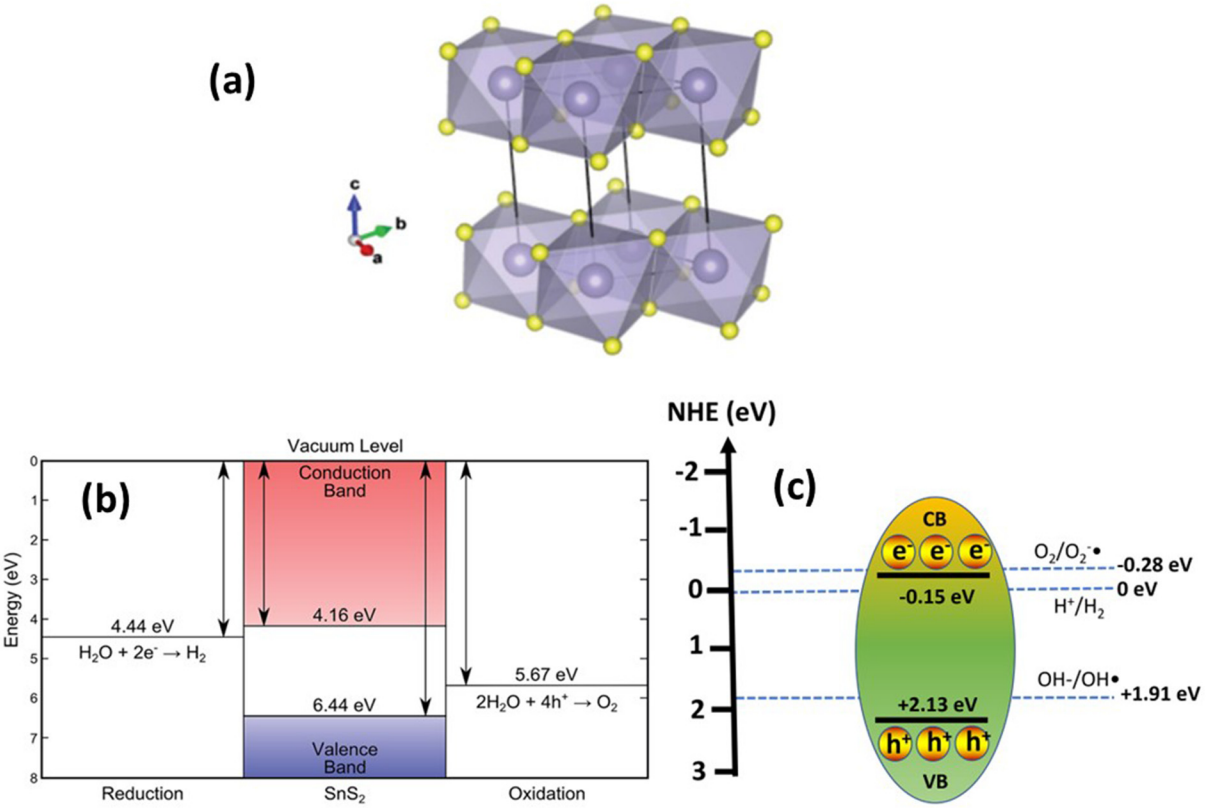

Fig. 2 (a) Crystal structure and (b) band position of SnS_2. (Reproduced from ref. 79 with permission from the Royal Society of Chemistry, copyright 2016.)[79] (c) Band position of SnS_2 for photocatalytic reactions.

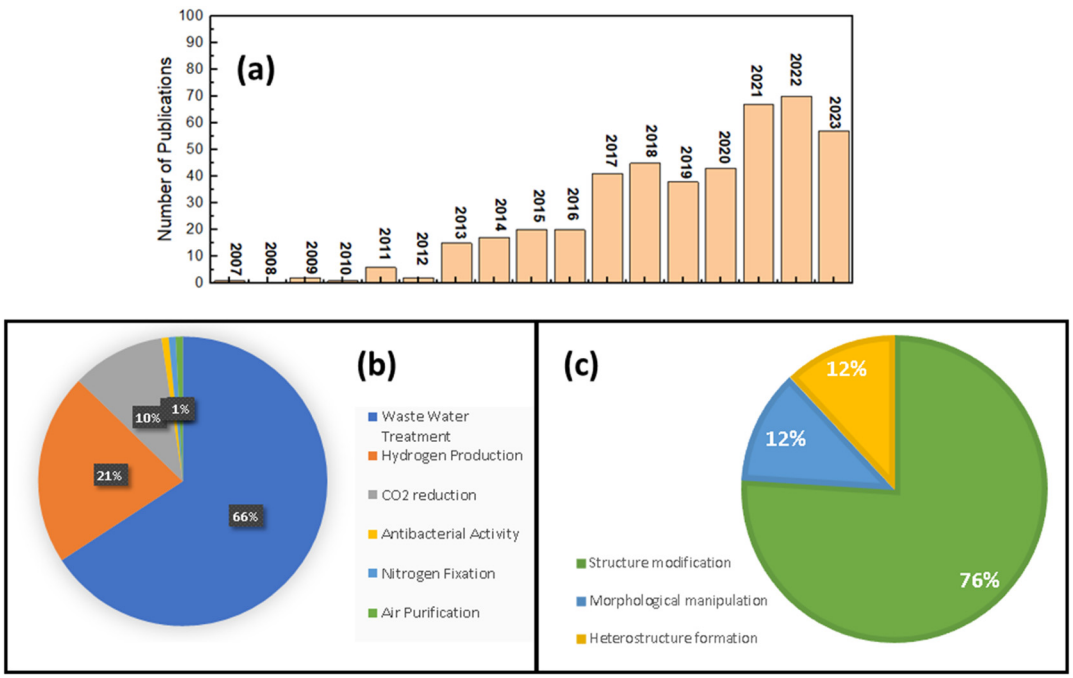

Fig. 3 (a) Number of SnS_2 photocatalytic publications; (b) summary of practical applications of SnS_2 photocatalytic. (c) Graphical illustration for photocatalytic improvement strategies for SnS_2.

ment under visible light irradiation and 192 of them are about organic dye removal such as methylene blue,[102–104] methyl orange,[105] and rhodamine B (RhB).[49,106] For heavy metals, hexavalent chromium (Cr(VI)) is the most studied waste water model for photocatalytic investigations of SnS_2, with 99 publications, which makes SnS_2 one of the most promising materials for Cr(VI) reduction under visible light irradiation. In the pharmaceutical waste field, tetracycline is the most studied wastewater, with 11 reports showing a good performance for tetracycline removal by a SnS_2 photocatalyst. Table 1 shows the summary of various types of application of SnS_2 photocatalysts. It can be seen that the SnS_2 photocatalyst exhibits great potential for various types of photocatalytic application.

2.2.1 CO_2 reduction. Recently, CO_2 conversion has attracted considerable attention for photocatalytic results due to its great potential for reducing CO_2 pollution alongside producing more valuable products.[107] Sun *et al.*[108] initiated efforts to reduce CO_2 through photocatalytic processes by SnS_2 under visible light irradiation. Their research successfully converted CO_2 into CO with a yield of approximately 80 ppm after 8 hours of xenon irradiation. Subsequently, Li *et al.*[109] explored the influence of SnS_2 morphology on CO_2 reduction *via* photocatalytic reactions. They examined two distinct morphologies —tablet-like and flower-like—and observed the conversion of CO_2 gas into CH_4 and CO gases. Notably, each morphology exhibited a unique behavior in CO_2 reduction. The flower-like morphology demonstrated a higher CH_4 yield at 97.5 μmol g^{-1} compared with CO gas at 75.1 μmol g^{-1}, while the tablet morphology showed stronger CO production at 61.6 μmol g^{-1} relative to CH_4 gas at 17.2 μmol g^{-1}. This underscores the impact of SnS_2 morphology on CO_2 reduction, which is directly linked to variations in charge separation processes, surface properties, and other factors (further elaborated in the subsequent discussion). Recent endeavors have focused on optimizing and enhancing CO_2 reduction through various techniques, including the formation of Z-scheme heterojunctions,[110] type II heterojunctions, vacancy generation,[106] and doping processes.[97] Among these strategies, Z-scheme heterojunctions have shown significant promise in improving the CO_2 reduction process. Wang *et al.* reported the synthesis of a Z-scheme photocatalyst, $SnO_2/SnS_2/Cu_2SnS_3$, which achieved a CO_2 reduction to ethanol rate of 28.44 mmol g^{-1} h^{-1} as a byproduct. The fundamental process of CO_2 reduction can be described as follows: when subjected to irradiation, electrons and holes are generated. Electrons in the conduction band, possessing a band position more negative than the reduction potential of CO_2, participate in reactions that transform CO_2 into various chemicals. The specific transformation depends on the suitability of the conduction band energy for reducing CO_2 into alternative chemical compounds.

2.2.2 Nitrogen reduction. The exploration of SnS_2 photocatalytic applications in nitrogen fixation is still relatively limited, with only four studies investigating its potential in this area. Li *et al.*[101] reported on the nitrogen fixation capability of SnS_2 using nanosheet and nanoplate morphologies. They found that the NH_4^+ concentration reached 40.5 μmol g^{-1} and 110.1 μmol g^{-1} on SnS_2-plate and SnS_2-sheet samples, respectively, after 4 hours, with average reaction rates of 10.1 μmol g^{-1} h^{-1} and 27.5 μmol g^{-1} h^{-1}, respectively. These findings highlight the sensitivity of SnS_2 photocatalytic performance to particle morphology. Three other reports discussed the nitrogen fixation application of SnS_2 in heterostructure forms. For instance, Nie *et al.*[92] demonstrated the formation of 1D/2D heterojunctions of SnS_2@MoO_3 as an efficient catalyst for visible photoelectric nitrogen fixation. Compared with pure MoO_3 and SnS_2, the nitrogen fixation performance improved by 2.3 and 4.6 times, respectively, and the Faraday efficiency was enhanced by 2.0 and 3.5 times, respectively. Another study by Lan *et al.*[94] also explored the formation of a Z-scheme heterojunction $Bi/Bi_2S_3/SnS_2$ for nitrogen fixation applications. The results showed that the Z-scheme formation of $Bi/Bi_2S_3/SnS_2$ successfully enhanced NH_4^+ production, yielding approximately 96.4 μmol g^{-1} h^{-1}, which is 1.9 and 3.0 times higher than that of SnS_2 and Bi/Bi_2S_3, respectively. The basic mechanism of the nitrogen fixation applications can be explained as follows: upon irradiation, the electrons and holes are generated. After that the photogenerated holes reacted with water to produce H^+ ions and in the final reaction N_2, H^+, and electrons reacted to produce NH_3 or NH_4^+ ions.[101]

2.2.3 H_2 production. Hydrogen production has become one of the popular applications for photocatalytic research since the growth of green sources of energy for switching from fossil fuels.[111] Initial investigations into the hydrogen production capabilities of SnS_2 were conducted in 2014. Yu *et al.*[45] prepared monodisperse SnS_2 nanosheets for hydrogen production under visible light irradiation, achieving a notable hydrogen production yield of approximately 0.566 mmol g^{-1} h^{-1}, which is considerably high for a visible light photocatalyst. The fundamental mechanism of H_2 production in photocatalytic reactions involving SnS_2 can be elucidated as follows: upon irradiation, the SnS_2 semiconductor generates electron–hole pairs. The photoexcited electrons reside in the conduction band and subsequently react with H^+ to produce H_2 gas. However, for the generation of H_2 gas, it is essential that the reduction potential of electrons in the conduction band exceeds the reduction potential of H^+/H_2 (0 V). The conduction band position of SnS_2 is influenced by various factors such as facet orientation and band gap. Huang *et al.*[69] demonstrated that the band position of SnS_2 is influenced by its facet orientation. Two facet orientations, (100) and (101), exhibit distinct performance characteristics in the photocatalytic production of H_2 gas. The (101) facet orientation is more favorable as it possesses a higher conduction band level than the reduction potential of H^+/H_2, whereas the dominance of the (100) facet results in a lower reduction potential in the conduction band compared with H^+/H_2. These findings suggest that the (101) facet of SnS_2 may be more conducive to H_2 production. Recent studies have focused on the development of S-scheme and Z-scheme photocatalysts (see Table 1) due to their efficient charge separation and band modulation properties.[112–117]

Table 1 Photocatalytic data of SnS_2 for various types of application

Sample	Sample	Light source	Photocatalytic result	Additional information	Ref.
CO_2 reduction	Cu-doped SnS_2	420 nm LED	CH_3OH yield 0.99 mmol g^{-1}		97
	S-vacancy SnS_2	400 W metal halide lamp	CO yield = 2.44 μmol g^{-1} h^{-1}. 1.48 times that of pure SnS_2		106
	SnS_2 flower-like	300 W xenon light	CO production rate 8.91 μmol g^{-1} h^{-1}		135
	Z-scheme SnO_2/SnS_2/Cu_2SnS_3	300 W xenon lamp	Ethanol yield 28.44 mmol g^{-1} h^{-1} 3 times higher than SnS_2		110
	SnS_2/SnO_2 nanoflower	300 W xenon lamp	CO yield 60.85 μmol g^{-1} h^{-1}		136
	Partly oxidized SnS_2	300 W xenon lamp	CO yield 12.28 μmol g^{-1} h^{-1}		67
	Carbon-doped SnS_2	300 W halogen lamp	CH_3CHO yield 125.66 μmol per 100 g per 3 h		67
	Carbon-doped SnS_2	150 W halogen lamp	CH_4 yield 0.64 μmol g^{-1} h^{-1}		67
	SnS_2 QDs/g-C_3N_4	300 W xenon lamp (420 nm cut-off)	CH_3OH yield 2.3 μmol g^{-1} h^{-1}		137
Hydrogen production	SnS_2-nanosheets	400 W mercury lamp	H_2 production rate: 0.566 mmol g^{-1} h^{-1}		31
	2.5 mol% Ni–SnS_2	400 W mercury lamp	1429 μmol g^{-1} h^{-1}		138
	In^{3+}-doped SnS_2	300 W xenon lamp	H_2 production rate: 470 mmol g^{-1} for 12 h		139
	S-scheme SnS_2/CdS	Simulated solar light (100 mW cm^{-2})	360.75 μL h^{-1}		116
	SnS_2/g-C_3N_4	300 W xenon lamp ($\lambda \geq$ 420 nm)	1818.8 μM g^{-1} h^{-1}		124
	SnS_2/CdS/TiO_2	300 W xenon lamp ($\lambda \geq$ 420 nm)	97.14 μmol h^{-1} cm^{-2}		140
	$SnS_2/BiVO_4$	100 mW cm^{-2} xenon lamp, 0.8 V	900 μmol cm^{-2}		117
	$SnS_2/Cd_{0.5}Zn_{0.5}S$	300 W xenon lamp ($\lambda \geq$ 420 nm)	3.19 mmol g^{-1} h^{-1}		141
Air purification	$Bi_4O_5Br_2$–SnS_2	Visible light	40% NO_x removal	NO_x abatement	44
	Ni-doped SnS_2/SnO_2	8 W, 256 nm light	85%	Trichloroethylene	54
	SnS_2/TiO_2	40 W fluorescence lamp	55% removal	Formaldehyde	55
Nitrogen fixation	SnS_2 nanosheets	330 W xenon lamp	27.5 μmol g^{-1} h^{-1}		101
	SnS_2/MoO_3	300 W xenon lamp	30.04 μg h^{-1} mg^{-1}		92
	$Bi/Bi_2S_3/SnS_2$	300 W xenon lamp	96.4 μmol g^{-1} h^{-1}		94
Antibacterial activity	SnS_2 nanoparticles	500 W xenon lamp	75.28 ± 2.3%	*S. aureus* (ATCC 25923)	41
	SnS_2 nanoparticles	500 W xenon lamp	78.95 ± 2.0%	*E. coli* (ATCC 13534)	41
	SnS_2 nanoparticles	500 W xenon lamp	81.22 ± 1.1%	*E. coli* (ATCC 25922)	41
	SnS_2	Visible light	50.39	*E. coli*	43
	Pr-doped SnS_2	Visible light	71.03	*E. coli*	43
Waste water treatment	SnS_2 nanoparticle	250 W xenon lamp ($\lambda \geq$ 420 nm)	k_{MO}: 0.0594 min^{-1}	Methyl orange	105
	MoS_2/SnS_2	Visible light	k_{MB}: 0.0594 min^{-1}	Methylene blue	122
	SnS_2 decorated biochar	Natural sunlight	k_{MB}: 0.013 min^{-1}	Methylene blue	142
	S–Sn–S vacancy SnS_2	300 W Xe lamp	k_{RhB} = 0.136 min^{-1}	Rhodamine B	143
	CdZnS/SnS_2/SnO_2	500 W xenon lamp	k_{RhB} = 0.0267 min^{-1}	Rhodamine B	49
	Zr-doped SnS_2	Larger than 420 nm	$k_{Cr(VI)}$ = 0.059 min^{-1}	Cr(VI)	144
	SnS_2 nanoparticle	300 W xenon lamp	$k_{Cr(VI)}$ = 0.00401 min^{-1}	Cr(VI)	129
	SnS_2@SnO_2	300 W xenon lamp	$k_{Cr(VI)}$ = 0.0907 min^{-1}	Cr(VI)	129
	SnS_2/SnS	Direct sunlight	$k_{Cr(VI)}$ = 0.086 min^{-1}	Cr(VI)	145
	SnS_2/CNTs	300 W xenon lamp ($\lambda \geq$ 420 nm)	$k_{Cr(VI)}$ = 0.07750 min^{-1}	Cr(VI)	146
	SnS_2 nanoplates	Solar irradiance was assumed to be 221 W m^{-2}	k_{TC} = 0.001 min^{-1}, k_{CP} = 0.0005 min^{-1}	Tetracycline and ciprofloxacin	134
	SnS_2/Bi_2WO_6	Solar irradiance was assumed to be 221 W m^{-2}	k_{TC} = 0.027 min^{-1}, k_{CP} = 0.024 min^{-1}	Tetracycline and ciprofloxacin	134
	SnS_2 nanoplates	Natural sunlight	k_{CP} = 0.0024 min^{-1}	Ciprofloxacin	132
	$SnS_2/BiVO_4$	Natural sunlight	k_{CP} = 0.018424 min^{-1}	Ciprofloxacin	132
	SnS_2 nanoplates	LED light 500 W m^{-2}	k_{GM} = 0.1492 min^{-1}	Gemifloxacin	37
	Platinum/polypyrrole–carbon black/SnS_2	LED light 500 W m^{-2}	k_{GM} = 0.0429 min^{-1}	Gemifloxacin	37
	SnS_2 nanoparticle	Visible light ($\lambda \geq$ 420 nm)	k_{TC} = 0.00129 min^{-1}	Tetracycline	38
	SnS_2/Bi_2MoO_{6-x}	Visible light ($\lambda \geq$ 420 nm)	k_{TC} = 0.01245 min^{-1}	Tetracycline	38
	SnS_2 nanoplates	Solar simulator	k_{NP} = 0.014 min^{-1}	Norfloxacin	147

2.2.4 Antibacterial activity. The SnS_2 photocatalyst has also been explored for antibacterial and antifungal applications. Fakhri *et al.*[41] demonstrated the removal of *S. aureus* (ATCC 25923), *E. coli* (ATCC 13534), and *E. coli* (ATCC 25922) with removal rates of 75.28 ± 2.3%, 78.95 ± 2.0%, and 81.22 ± 1.1%, respectively. The basic mechanism of antibacterial removal by SnS_2 nanoparticles can be elucidated as follows: upon irradiation, electrons and holes are generated, and the photogenerated holes and electrons react with OH^- and O_2 to produce $^{\bullet}OH$ and $O_2^{\bullet-}$, respectively. These radical species are then converted into H_2O_2, serving as potent oxidative agents for killing bacterial cells. In another study, Fakhri *et al.*[118] investigated the impact of heterojunction formation of SnS_2/SnO_2 on antibacterial and antifungal activity. Their results indicate that SnS_2/SnO_2 exhibits superior bacteria-killing ability compared with pure SnS_2 and SnO_2, possibly due to the inhibition of the charge carrier separation of electrons and holes. Furthermore, antifungal activity was assessed against pathogenic *C. albicans*. The largest zones of inhibition for the control, SnO_2 nanoparticles, SnS_2 nanoplates, and SnO_2/SnS_2 nanocomposite are 5.89 mm, 13.20 mm, 14.01 mm, and 21.11 mm, respectively. A recent study by Ech-Chergui *et al.*[43] has corroborated the antibacterial activity of Pr-doped SnS_2 for combating *E. coli*. The Pr-doped SnS_2 exhibits enhanced bacteria-killing activity compared with SnS_2 alone, attributed to the smaller crystallite size providing more active sites for photocatalytic reactions.

2.2.5 Air purification. One of the major environmental issues is the deterioration of air quality due to heavy industry. Various types of air pollutant, including NO_x gas, VOCs, and other gases, are released into our environment, leading to serious health problems. Photocatalytic technology has been acknowledged as one of the solutions to address this issue.[119] In the case of SnS_2 photocatalysts, SnS_2 has been reported to effectively remove various types of air pollutant, including NO_x gas, formaldehyde, and trichloroethylene, as shown in Table 1. However, the number of reports on the use of SnS_2 for air purification is very low, with fewer than 10 publications available. Moreover, all these reports involve heterojunction formation. Therefore, for further development, it is necessary to investigate the use of SnS_2 alone for this application.

2.2.6 Waste-water

2.2.6.1 Organic dyes. Organic dyes are prevalent pollutants in wastewater within our immediate environment, often originating from direct discharge by the textile industry, presenting significant environmental concern. Utilizing photocatalytic wastewater treatment emerges as a promising solution to address this issue, offering notable advantages such as cost-effectiveness, simplicity, and the capability to convert the chemical composition of organic dyes into harmless byproducts such as CO_2.[120,121] In the realm of employing SnS_2 as a photocatalyst for organic dye degradation, extensive research has been conducted, targeting various dye types including methylene blue,[122] methyl orange,[123] rhodamine B,[124–126] crystal violet,[127] and others. Table 1 depicts the efficacy of SnS_2 photocatalysts in removing organic dyes. Notably, the data demonstrate promising outcomes across all the tested dyes. The underlying mechanism of organic dye degradation can be elucidated as follows: upon irradiation, electron–hole pairs are generated, which subsequently react with O_2 and OH^- to yield highly reactive $O_2^{\bullet-}$ and $^{\bullet}OH$ radicals. These radicals possess strong oxidative capabilities, facilitating the decomposition of diverse synthetic dyes into CO_2 and water.

2.2.6.2 Heavy metals. In addition to organic dyes, the reduction of heavy metals represents a significant area of study in the photocatalytic application of SnS_2. Among various heavy metals, hexavalent chromium (Cr(VI)) has been extensively researched. Several strategies have been developed to enhance Cr(VI) removal, including vacancy generation,[48] doping formation,[128] and heterostructure formation.[129] The basic mechanism of Cr(VI) reduction involves the generation of electrons and holes upon irradiation, where the photoexcited electrons can directly decompose Cr(VI) ions into Cr(III). The photocatalytic ability of SnS_2 depends on the extent to which electrons react with Cr(VI) molecules, which may be attributed to increasing active sites or improving charge carrier separation efficiency. Table 1 presents several studies confirming the degradation of Cr(VI) using SnS_2 photocatalysts with varying capabilities. A detailed analysis will be provided in the subsequent section.

2.2.6.3 Antibiotics. Pharmaceutical waste, including compounds like tetracycline and others, presents a significant challenge in wastewater management, particularly with many pharmaceutical industries directly discharging their waste into water bodies. Consequently, effective treatment methods are imperative to mitigate the presence of these hazardous chemicals in water. Photocatalysis has emerged as a promising technique for efficiently removing pharmaceutical waste from water. However, the utilization of SnS_2 photocatalysts for antibiotic removal remains limited. Only a small number of research papers, fewer than 30, have explored the use of SnS_2 photocatalysts for this purpose, with most focusing on the formation of heterojunctions with SnS_2, such as Z-scheme and S-scheme configurations.[42,104,130,131] For instance, Kumar *et al.*[132] demonstrated the effectiveness of Z-scheme SnS_2/$BiVO_4$ in removing the antibiotic ciprofloxacin from aqueous solutions. They found that the optimized batch with 0.15SnS_2/$BiVO_4$ exhibited a significantly higher apparent rate constant (k = 0.0184 min^{-1}) compared with $BiVO_4$ (k = 0.0049 min^{-1}) and SnS_2 (k = 0.0024 min^{-1}) alone. This improved performance was attributed to enhanced charge separation efficiency, enabling electrons from SnS_2 to directly react with O_2 to form $O_2^{\bullet-}$, ultimately degrading ciprofloxacin into CO_2 and water.[133] Other antibiotics have also been shown to be degradable by SnS_2 photocatalysts. For example, Kumar *et al.*[134] reported the use of SnS_2/Bi_2WO_6 for the removal of ciprofloxacin and tetracycline. While SnS_2 alone exhibited minimal removal capabilities for these antibiotics, the combination with Bi_2WO_6 significantly enhanced the degradation rates. These findings suggest that SnS_2 photocatalysts alone are insufficient for effectively decomposing various types of pharmaceutical waste. One of the key limitations is the rapid recombination of electron–hole

pairs, which impedes the reaction of electrons with O_2 to generate reactive oxygen species (ROS). Therefore, the development of hybrid photocatalytic systems, combining SnS_2 with other materials, holds promise for improving the efficiency of pharmaceutical waste removal from wastewater. Continued research in this area is crucial for advancing sustainable water treatment technologies.

Although there are many publications about photocatalytic performance with different applications, we can categorize their strategies into three different categories.

(1) Structural modification: This strategy involves altering the structure of SnS_2 to enhance its photocatalytic properties. This could include changes in the composition, arrangement of atoms, or other structural aspects.

(2) Morphological manipulation: Morphological manipulation focuses on changing the physical shape or form of SnS_2 to improve its photocatalytic performance. This might involve controlling the particle size, shape, or surface structure.

(3) Heterostructure formation: This approach involves creating composite materials by combining SnS_2 with other materials, possibly forming interfaces or layered structures. The high percentage suggests that researchers find this strategy particularly effective or promising for enhancing photocatalytic performance.

Based on these three classifications, the quantitative analysis has been made and plotted in Fig. 3(c) based on the Scopus data until now. The structural modification and morphological manipulation SnS_2 strategies are just 12% each of the total of publications of SnS_2 photocatalytic. On the other hands, the heterostructure formation exceeded more than 75%, which indicates, at the current stage, that the heterostructure formation of SnS_2 is the most popular strategy for improving strategies, which probably attributed to the unique characteristics of composite structures which imply to the better performance.

3 Photocatalytic improvement strategies

3.1 Structural modification

Structural modification is a valuable strategy for enhancing photocatalytic performance. By adjusting the structural properties of the photocatalyst, it is possible to improve its electronic and surface characteristics for a range of photocatalytic applications, including optimizing light utilization, enhancing charge transfer kinetics, and creating additional active sites.[148,149] Several established techniques can be employed to modify the structure of the photocatalyst, including vacancy generation and doping. These methods can increase the photocatalyst's charge separation efficiency and surface reactivity by raising the adsorption energy.

3.1.1 Vacancy generation. Vacancies in 2D materials, such as graphene and transition metal dichalcogenides (TMDs), have garnered significant attention due to their easy formation in these materials. In addition to expediting the charge separation, the generation of vacancies in 2D materials like SnS_2 can increase the number of active sites, facilitating reactant adsorption and thereby implying photocatalytic improvements. In the case of SnS_2, sulfur vacancies have been well established as effective methods for modifying its structure in photocatalytic applications.

The synthesis of sulfur vacancy-generating SnS_2 was reported by Qiang *et al.*,[48] prepared *via* hydrothermal reaction for Cr(VI) reduction under visible light irradiation. They observed that adjusting the molar ratio between the Sn and S precursors during synthesis is crucial for controlling the defect concentration on SnS_2 nanoparticles. A higher Sn to S ratio indicates a higher defect content, confirmed by EPR analysis (Fig. 4(a)). An intense resonance signal from EPR analysis for the sample with a Sn to S ratio of five was observed, indicating a higher defect concentration compared with the sample with a lower Sn to S ratio due to sulfur vacancy. Photocatalytic Cr(VI) reduction also demonstrated that the sample with a high defect content exhibits the best photocatalytic ability (Fig. 4(b)). This phenomenon was attributed to the prolonged charge carrier lifetime of the sulfur vacancy sample, as demonstrated in the photocurrent analysis of all the prepared samples (Fig. 4(c)). SnS_2 nanosheets with an optimal amount of sulfur vacancies exhibited a superior photoreduction rate of Cr(VI) (100% in 20 min), roughly 18.09 times higher than that of pure SnS_2 (Table 2), indicating vast prospects for photocatalytic wastewater treatment. The presence of sulfur vacancies in the crystal structure of SnS_2 serves to create an electron trap between the valence band and conduction band, effectively slowing down the recombination of electrons and holes. In that case the trapped electrons are still able to generate chemical reactions with Cr(VI) ions to change into less hazardous ions (Cr(III)).

Sulfur vacancy generation is not only suitable for Cr(VI) reduction but also for other applications, including CO_2 reduction and phenol degradation. In a recent publication, Zhang *et al.*[150] employed a synthesis method using L-cystine as the sulfur precursor to generate S-vacancies in SnS_2 for CO_2 reduction (see Fig. 4(d)). Their investigation demonstrated a significant enhancement in the CO_2 reduction efficacy of SnS_2 with S-vacancies, showcasing a 14.3-fold improvement compared with commercially available SnS_2 products. Their objective was to elucidate the underlying mechanism of CO_2 reduction and discern the role of Sn^0 atoms in CO_2 adsorption. Through DFT analysis, it was observed that the CO_2 molecule approached the surface of Sn/SnS_2, where the S_x^{2-} ions in proximity transferred photogenerated electrons to the oxygen atom of the CO_2, thereby activating the CO_2 molecule and facilitating adsorption. Sn^0 particles functioned as electron transport bridges, enabling the further transfer of photogenerated electrons to the S_x^{2-} ions, consequently reducing the adsorption energy barrier and accelerating the reaction rate. In a parallel investigation, Li *et al.*[106] explored variations in the Sn precursor's valence state (Sn^{2+} and Sn^{4+}) to induce S-vacancies in the crystal structure. Based on their investigation, the Sn^{2+} precursor yielded a higher S-vacancy content than the Sn^{4+} precur-

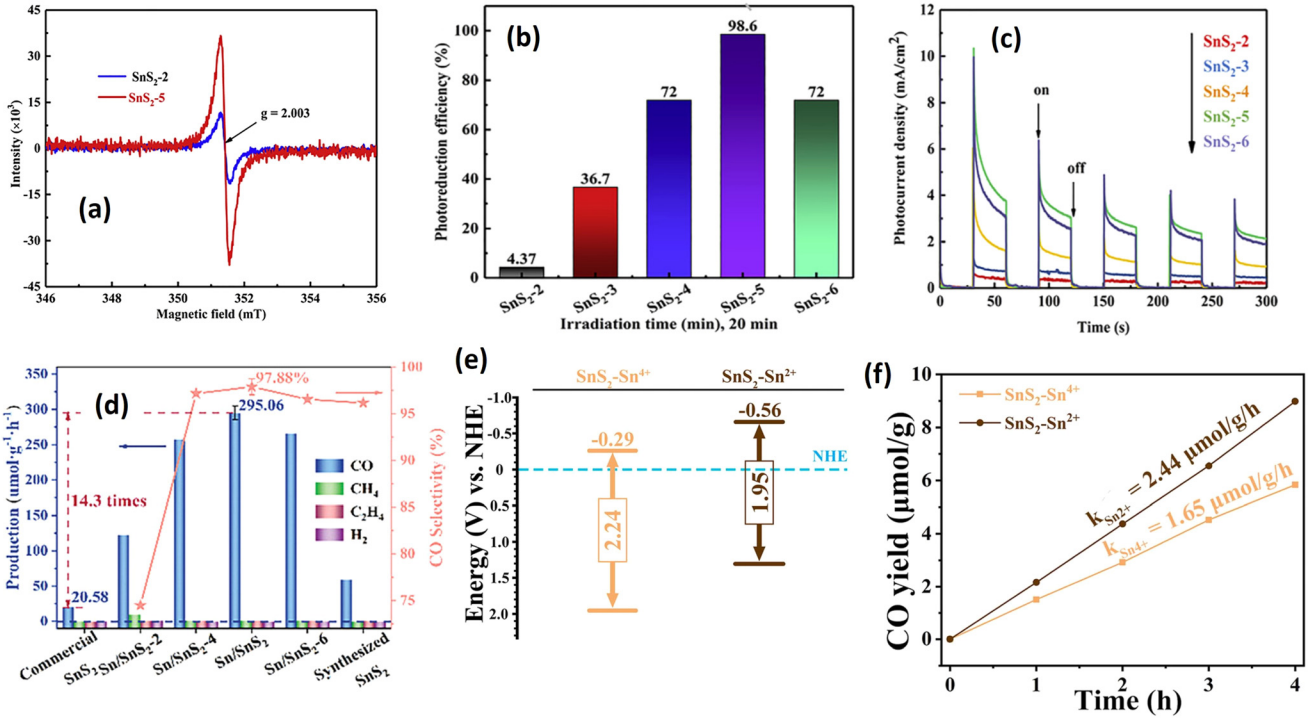

Fig. 4 (a) Room-temperature EPR spectra of SnS_2-2 and SnS_2-5. (b) Comparison of Cr(VI) photoreduction over SnS_{2-X} (X = 2, 3, 4, 5, 6) under visible light irradiation. (c) Photocurrent response of SnS_{2-X} (X = 2, 3, 4, 5, 6).[48] (Reproduced from ref. 48 with permission from Elsevier, copyright 2020.) (d) Photocatalytic CO_2 reduction performance of vacancy generated SnS_2 prepared at different L-cystine concentrations (−1, −2, −4, −6 mol).[150] (Reproduced from ref. 150 with permission from Wiley, copyright 2023.) (e) Energy band of SnS_2–Sn^{4+} and SnS_2–Sn^{2+}. (f) CO_2 reduction of SnS_2–Sn^{4+} and SnS_2–Sn^{2+}.[106] (Reproduced from ref. 106 with permission from Elsevier, copyright 2023.)

sor, with a determined vacancy ratio (*via* EPR analysis) of 4 : 1 for Sn^{2+} : Sn^{4+}. This increase in S-vacancy quantity resulted in a band position shift, as illustrated in Fig. 4(e), leading to a more potent CO_2 reduction capability. Photocatalytic CO_2 reduction revealed a 1.47 times enhancement with the Sn^{2+} precursor compared with Sn^{4+}, attributed to the heightened S-vacancy concentration (see Fig. 4(f)). The enhanced photocatalytic performance following an increase in S-vacancy concentration can be attributed to several factors, including improved light absorption and increased efficiency in the separation of photogenerated charge carriers. Beyond S-vacancies, other vacancy types, such as Sn–S vacancies and S–Sn–S vacancies, may exist, imparting distinct effects on the physical properties and photocatalytic performance of SnS_2. Guo *et al.*[143] addressed these defects by introducing a specific amount of 2,2′-bipyridine during the hydrothermal reaction. Their research has confirmed several phenomena directly correlated with the improvements in photocatalysis. The presence of S-vacancies and S–Sn–S vacancies could decrease the band gap energy, resulting in an upward shift of the valence and conduction bands. This shift facilitates a stronger reduction ability, enabling more efficient reactions with O_2 molecules. Furthermore, the S–Sn–S vacancy demonstrates the highest adsorption energy, followed by Sn–S and S vacancies, respectively. This trend is also reflected in the electron transfer ability, with the S–Sn–S vacancy exhibiting an electron transfer ability 4.7 times higher than that of S vacancy. These findings suggest that the presence of S–Sn–S vacancies is more favorable for improving photocatalytic performance, a conclusion also supported by Guo *et al.*[143] for phenol decomposition (Table 2).

3.1.2 Doping SnS_2. Doping is widely recognized as an effective method for altering the structure of photocatalysts to improve their photocatalytic performance. In the case of SnS_2, the doping process involves the replacement of one or more SnS_2 atoms with other atoms, including cations or anions. Transition metal elements such as Cu,[97,151] Ce,[152] Zr,[144] and others have been successfully integrated into the SnS_2 structure. For instance, Liu *et al.*[153] demonstrated the doping of Cu onto the SnS_2 layer *via* a hydrothermal reaction for H_2 production applications under visible light irradiation. They varied the Cu concentration from 0 to 10% to determine the optimal concentration. The results indicated that a 5% Cu concentration represented the optimal condition for water-splitting photocatalytic reactions, exhibiting a sixfold increase compared with 0% Cu, as depicted in Fig. 5(a). Interestingly, the Cu doping process induces defects in the crystal structure of SnS_2, as investigated by EPR analysis, as depicted in Fig. 5(b). The electron paramagnetic resonance (EPR) signal for Cu-doping exhibits a stronger signal than undoped SnS_2, confirming the presence of a vacancy defect originating from the S-vacancy. This result indicates that a S-vacancy can be gener-

Table 2 Summary of photocatalytic performance through vacancy engineering and doping formation of SnS_2

Vacancy type	Light source	Photocatalytic testing	Photocatalytic performance	Ref.
S-vacancy SnS_2	500 W Xe lamp	50 mg L^{-1} Cr(VI) reduction	Degradation efficiency (100% in 20 min), roughly 18.09 times that of pure SnS_2	48
S-vacancy SnS_2	400 W metal halide lamp	(1×10^{-5} M) rhodamine B (RhB) degradation	k_{RhB} = 0.0102 min^{-1} for S-vacancy SnS_2, ~2.1 times that of SnS_2	106
S-vacancy SnS_2	400 W metal halide lamp	CO_2 reduction (1 atm)	CO yield = 2.44 μmol g^{-1} h^{-1}. 1.48 times that of pure SnS_2	106
S–Sn-vacancy SnS_2	300 W Xe lamp	RhB, and methylene blue (MB) degradation	k_{RhB} = 0.054 min^{-1} (3.17 times that of pure SnS_2), k_{MB} = 0.043 min^{-1} (3.07 times that of pure SnS_2)	143
S–Sn–S-vacancy SnS_2	300 W Xe lamp	RhB and MB degradation	k_{RhB} = 0.136 min^{-1} (8.00 times that of pure SnS_2), k_{MB} = 0.116 min^{-1} (8.28 times that of pure SnS_2)	143
C-doped SnS_2	Visible light	CO_2 reduction (acetaldehyde formation)	Acetaldehyde formation: 1256.6 μmol g^{-1} (228.47 times that of SnS_2)	67
Cu-doped SnS_2	420 nm LED	CO_2 reduction (CH_3OH production)	Cu-doped SnS_2: 0.99 mmol g^{-1} h^{-1} (2.06 times that of SnS_2)	97
Cu-doped SnS_2	300 W xenon lamp	Hydrogen evolution	Cu-doped SnS_2: 1.37 mmol g^{-1} h^{-1} far exceeding 6 times that of pure SnS_2	153
Ce-doped SnS_2	Solar irradiation	10 and 20 ppm of methyl orange (MO)	k_{MO} = 0.096 and k_{MO} = 0.080 for 10 ppm and 20 ppm. SnS_2: k_{MO} = 0.045 and k_{MO} = 0.035 for 10 and 20 ppm	87
Zr-doped SnS_2	Larger than 420 nm	40 mg L^{-1} Cr(VI) reduction	$k_{Cr(VI)}$ = 0.059 min^{-1} nearly 2.2 times that of SnS_2	144
In^{3+}-doped SnS_2	White LED 48 W	20 ppm Cr(VI) reduction	$k_{Cr(VI)}$ = 0.123 min^{-1}. 39.4 times that of SnS_2	128
In^{3+}-doped SnS_2	300 W xenon lamp	Hydrogen evolution	H_2 production rate: 470 mmol g^{-1} for 12 h. 1.95 times higher than SnS_2	139
Sr-doped SnS_2	250 W xenon lamp	10 ppm RhB degradation	k_{RhB} = 0.00721 min^{-1} (1.55 times that of SnS_2)	154

ated not only by controlling the S-source but also through the doping process. Moreover, the average electron lifetime of Cu-SnS_2 is longer than SnS_2, as shown in Fig. 5(c). The average lifetime of Cu-doped SnS_2 is 0.358 s, which is slower than SnS_2, with 0.341 s, indicating that defects caused by the S-vacancy act as electron acceptors, preventing electron and hole recombination. Upon exposure to visible light irradiation, electrons transition from the valence band to the conduction band. As defects are introduced, these electrons migrate to defect levels and promptly engage in reactions with adsorbed H_2O, rather than undergoing recombination with holes in the valence band. Additionally, compared with pristine SnS_2, Cu doping enables a broader range of visible light absorption, suggesting increased electron involvement in the redox reaction. Furthermore, due to the vacancies generated by Cu doping, the crystallinity decreases, and surface area increases. These factors are also beneficial for enhancing the photocatalytic reaction. Another study by Govindan *et al.*[87] conducted successful cation doping, introducing Ce atoms into the SnS_2 structure using a microwave-assisted method. In their research, they observed the formation of Sn-vacancies instead of S-vacancies. Additionally, alongside S-vacancy formation, they noted an increase in strain on the crystal structure of SnS_2 after Ce doping, measuring approximately 3.5×10^{-3}, which was higher than without Ce doping (2.3×10^{-3}). This behavior can be attributed to the higher atomic radius of Ce^{3+}/Ce^{4+} (0.102 nm) compared with Sn^{4+} (0.07 nm). The modification of the SnS_2 structure with Ce doping was confirmed to enhance the photocatalytic performance, demonstrated by conducting methyl orange degradation under solar irradiation. The results indicate that Ce-doped SnS_2 improved the degradation of methyl orange twice as fast as pristine SnS_2 (Table 2). The higher photocatalytic performance of Ce-doped SnS_2 could be attributed to the decreased crystallite size resulting from significant strain and a greater quantity of Sn vacancies. These factors facilitate a greater number of photon pathways within the SnS_2 host structure, consequently enhancing the photocatalytic activity for decomposing methyl orange molecule into CO_2 and water. In contrast to the above analysis, Park *et al.*[128] proposed a different mechanism to explain the doping behavior of In^{3+}-doped SnS_2. They proposed that instead of the S-vacancy serving as an electron acceptor, the In^{3+} ions serve as electron acceptors, effectively improving the charge carrier separation efficiency as shown in Fig. 5(d). The photocurrent analysis of In^{3+}-SnS_2 shows strong photoelectron excitation compared with SnS_2, which is directly correlated with the luminescence analysis in Fig. 5(e), indicating a slower recombination of electrons and holes after In^{3+} doping. The photocatalytic activity of In^{3+}-doped SnS_2 tested for Cr(VI) reduction (Fig. 5(f)) shows a superior performance compared with SnS_2 and standard P-25 under visible light irradiation, providing clear evidence of the effect of In^{3+} in enhancing photocatalytic performance through extending the electron–hole lifetime. However, the effect of In^{3+} has been strengthened by Li *et al.*[139] who proposed that In^{3+} is responsible for S-vacancy generation, acting as an electron trap to improve hydrogen generation, with a hydrogen production rate of about 470 μmol g^{-1} for 12 h as shown in Table 2.

Doping in SnS_2 structures, not only within the transition metal family but also through carbon infusion, has been demonstrated to markedly enhance photocatalytic efficacy. In a study by Shown *et al.*,[67] carbon-doped SnS_2 was investigated

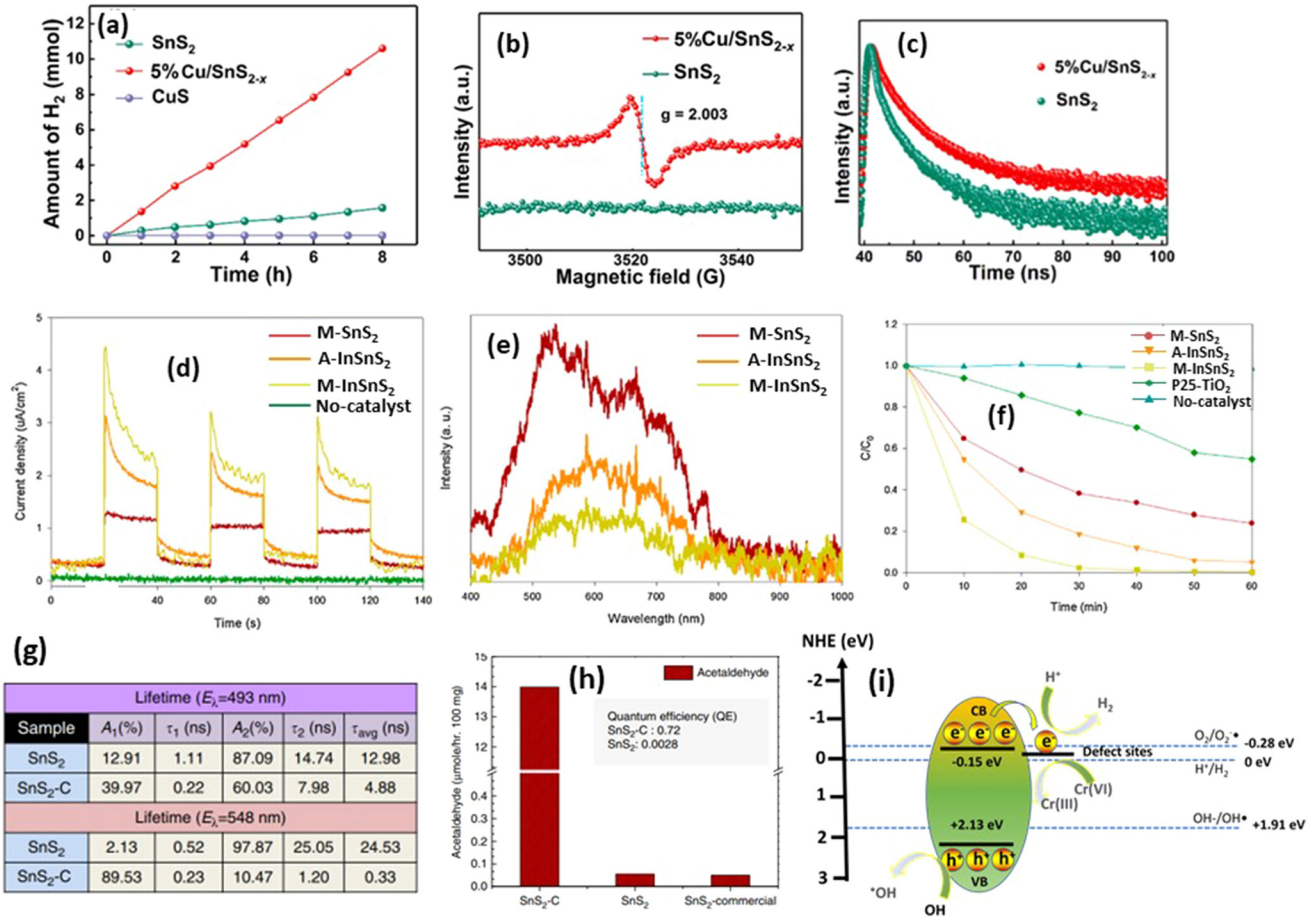

Lifetime (E_λ=493 nm)					
Sample	A_1(%)	τ_1 (ns)	A_2(%)	τ_2 (ns)	τ_{avg} (ns)
SnS_2	12.91	1.11	87.09	14.74	12.98
SnS_2-C	39.97	0.22	60.03	7.98	4.88
Lifetime (E_λ=548 nm)					
SnS_2	2.13	0.52	97.87	25.05	24.53
SnS_2-C	89.53	0.23	10.47	1.20	0.33

Fig. 5 (a) Photocatalytic water reduction capability of SnS_2, CuS, and Cu-doped SnS_2. (b) EPR spectra of SnS_2 and Cu-SnS_2, and (c) time-resolved photoluminescence spectra of SnS_2 and Cu-doped SnS_2.[97] (Reproduced from ref. 97 with permission from the Royal Society of Chemistry, copyright 2023.) (d) Photocurrent measurements of In^{3+}-doped SnS_2. (e) Photoluminescence measurement of In^{3+}-doped SnS_2. (f) Cr(VI) photodegradation by using In^{3+}-doped SnS_2.[128] (Reproduced from ref. 128 with permission from Elsevier, copyright 2017.) (g) Charge life-time of C-doped SnS_2. (h) Photocatalytic CO_2 reduction into acetaldehyde by using carbon-doped SnS_2.[67] (Reproduced from ref. 67 with permission from Springer Nature, copyright 2018.) (i) Photocatalytic reaction mechanism of S-vacancy on the SnS_2 structure.

for its capacity to catalyze CO_2 reduction to acetaldehyde gas under 300 W halogen irradiation. The carbon doping regimen involved the use of L-cystine as both a sulfur and carbon source. The results revealed that carbon doping induced macrostrain within the SnS_2 lattice, leading to distinct photophysical properties. Moreover, carbon doping facilitated the adsorption of CO_2 molecules on the surface, with a relatively low dissociation barrier observed. In Fig. 5(g), the observed average lifetimes for SnS_2–C are 4.88 and 0.33 ns, markedly shorter than the 12.98 and 24.53 ns for SnS_2 at 493 and 548 nm, respectively. This decrease in lifetime in SnS_2–C implies the presence of a nonradiative pathway, characterized by the delocalization of electrons from SnS_2 to C, thereby facilitating effective carrier separation. Additionally, the resulting carbon-doped SnS_2–C exhibited smaller nanosheets composed of only a few atomic layers, thereby reducing the charge diffusion times compared with pure SnS_2. These findings collectively underscore the exceptional quantum efficiency of carbon-doped SnS_2, which demonstrated an improvement of over 257 times compared with pristine SnS_2. This enhanced quantum efficiency manifested as a remarkable increase in acetaldehyde production on carbon-doped SnS_2, outperforming pure SnS_2 by 228.47 times (Fig. 5(h)).

Based on the results, structural modification can enhance photocatalytic performance by several factors including S-vacancy generation, strain engineering, and ion trapping which successfully impeded the recombination of electrons and holes through an electron trap. However, since the majority of the publications state that the S-vacancy was the most responsible species for improving the photocatalytic reaction, therefore the photocatalytic mechanism of SnS_2's structural modification can be generally explained as follows (Fig. 5(i)): upon exposure to light, electrons from the valence band become excited to the conduction band of SnS_2. Without a vacancy state, the electron would easily recombine with holes in the valence band. However, due to the presence of a vacancy state below the conduction band of SnS_2, electrons tend to be trapped, providing sufficient time to initiate photocatalytic

reactions. These reactions have potential applications in various fields, including hydrogen production, wastewater treatment, and many others.

All these structural modification strategies exhibit varying degrees of improvement in photocatalytic applications, as summarized in Table 2. Among these strategies, the carbon doping of SnS_2 emerges as one of the most promising approaches, showing an enhancement ability over 228.47 times greater than pristine SnS_2 in the reduction of CO to acetaldehyde.[67] Additionally, In^{3+} doping in the SnS_2 structure demonstrates a superior photocatalytic performance for wastewater treatment, exhibiting an improvement degree approximately 39.4 times higher than pristine SnS_2.[128] This suggests that In^{3+} doping enhances the charge separation efficiency more effectively than other cation doping methods and direct S-vacancy formation. However, the underlying mechanisms of this phenomenon remain unclear, as each doping process generates S-vacancies in the system, and the role of the dopant itself is not fully understood. Therefore, one plausible explanation for this phenomenon may lie in the variation in vacancy content and surface properties of the SnS_2 after doping, including an increased surface area and other factors.

3.2 Morphological manipulation

Beyond the structural factor, the photocatalytic activity of SnS_2 is also influenced by its surface properties. These properties are intricately linked to changes in morphology, impacting the surface area, the active facets, and the reaction process for photocatalytic reactions. Researchers have explored various SnS_2 morphologies, each demonstrating distinct photocatalytic performances. These morphologies encompass flower-like structures, nanosheets, nanoparticles, quantum dots, and more.

3.2.1 Flower-like. The flower-like morphology of SnS_2 is one of the most common shapes observed. It is formed due to the arrangement of several hexagonal shapes, creating a flower-like structure, as shown in Fig. 6(a).[155] This shape is typically prepared through a direct hydrothermal reaction without additional surfactants. The size of the flower can be adjusted by varying the reaction conditions, such as reaction time, temperature, and precursor amounts. One advantage of the flower-like morphology is the abundance of active sites on the crystal structure's edges.[156] Sengodu *et al.*[157] have successfully synthesized three distinct morphologies of SnS_2: nano-

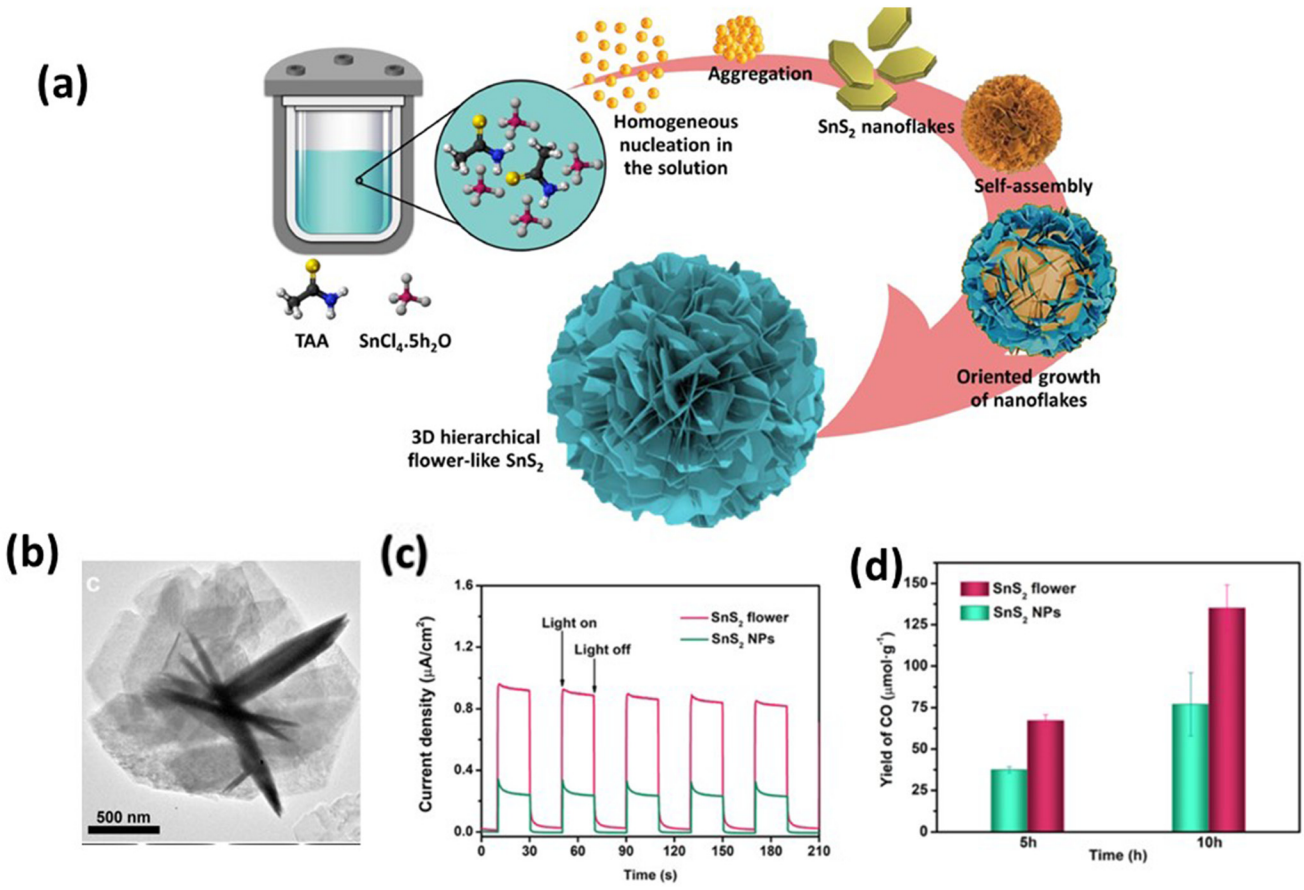

Fig. 6 (a) Formation of SnS_2 rose flower-like morphology.[155] (Reproduced from ref. 155 with permission from Elsevier, copyright 2021.) (b) TEM images of an individual SnS_2 flower. (c) Transient photocurrent and (d) comparative CO formation yield of the SnS_2 flower and SnS_2 NPs within the reaction times of 5 and 10 h, respectively.[135] (Reproduced from ref. 135 with permission from the American Chemical Society, copyright 2021.)

particles, nanoflowers (flower-like), and nanoplates, each exhibiting unique specific surface areas. Notably, the nanoflower morphology stands out with the highest specific surface area recorded, at 127.04 $m^2\ g^{-1}$, surpassing the values for nanoplates and nanoparticles, which are 96.40 and 69.4 $m^2\ g^{-1}$, respectively. Mondal *et al.*[158] corroborated the superior photocatalytic performance of the flower-like morphology, emphasizing its potential for environmental applications. Their study revealed that controlling the sulfur source precursor, particularly employing 0.06 g thioacetamide, led to the formation of nanoflowers, while 0.1 g thioacetamide resulted in a distinct nano-yarn morphology. Moreover, the nanoflower morphology of SnS_2 exhibited a markedly higher specific surface area than the nano-yarn, proving advantageous for enhanced photocatalytic Cr(VI) reduction under visible light irradiation. Upon photocatalytic reactions, the nanoflower with a high specific surface area can absorb more molecules onto the surface, increasing the likelihood of reaction occurrence. Moreover, the higher specific surface area enhanced light absorption leading to a more efficient generation of electron and holes for reducing C(VI) into Cr(III). Another report from You *et al.*[135] has investigated the advantages of a flower-like morphology over nanoparticles. They observed that the flower-like structures prepared by the hydrothermal reaction have an average size of 2.39 ± 0.26 μm and a thickness of around 20 nm, which is favorable for carrier transport to the catalyst surface (Fig. 6(b)). The flower-like morphology has a surface area around 20.11 $m^2\ g^{-1}$ which is higher than for the nanoparticle, at 12.99 $m^2\ g^{-1}$. Hence, SnS_2 flowers can supply more surface-active sites, leading to higher adsorption and photocatalysis. The flower-like structure also can absorb more light, as illustrated in Fig. 6(c), due to the scattering and reflection of light within the three-dimensional structure. Also, a thin sheet structure can shorten the transmission path, promoting more carriers to migrate to the surface of the photocatalyst.[135] The photocatalytic CO_2 reduction performance is undoubtedly directly correlated with the properties, as shown in Fig. 6(d). The CO_2 reduction performance of the flower-like morphology is 135.13 μmol g^{-1} which is 1.75 times higher than SnS_2 nanoparticles.

3.2.2 2D nanosheets. Two-dimensional (2D) layered morphologies can be defined as morphologies with a large two-dimensional ratio and a low vertical ratio. Due to their unique physicochemical properties, 2D material-based photocatalysts are expected to offer intriguing features such as porous structures, high specific surface areas, good crystallinity, a rich variety of host–guest species, better charge carrier separation, and abundant surface-active sites.[159] As mentioned earlier, the TMD family exhibits 2D properties, providing an advantage for photocatalytic applications. In the case of the SnS_2 photocatalyst, several reports have successfully demonstrated the preparation of 2D layered structures for photocatalytic applications.[45,71,160–163] Yu *et al.*[45] have reported monodisperse SnS_2 nanosheets for hydrogen generation photocatalysis. Fig. 7 (a and b) shows the SnS_2 hexagonal nanosheets of 0.8–1 μm with a thickness of about 22 nm. The nanosheets are assembled by *ca.* 35–38 hexagonal SnS_2 layers (the experimental value of single-layer SnS_2 is determined to be 0.61 nm). Yu *et al.*[45] prepared the SnS_2 nanosheets using a hydrothermal method with polyvinyl pyrrolidone (PVP) as a controlling agent. PVP can act in aggregation prevention during the hydrothermal reaction, preventing the SnS_2 layers from stacking into flower-like morphologies. Moreover, the monodisperse SnS_2 layers can also be achieved in an ethanol solution. The photocurrent measurement indicates that SnS_2 nanosheets have high electron mobility, which is beneficial for the H_2-production reaction compared with the P-25 standard (Fig. 7(c)). The H_2-production testing result shows various morphologies that have been compared with SnS_2 nanosheets, including nanoplates and sphere particles. The H_2 production yield for the nanosheet sample is much higher than for nanoplates, and spheres, as well as P-25 (Fig. 7(d)). The enhanced photocatalytic activity of SnS_2 nanosheets may be attributed to their low thickness, which provides more active sites. Additionally, their short and convenient approach allows photogenerated electrons and holes to migrate efficiently to the reaction sites on the surface, thereby decreasing the recombination probability and enhancing the photocatalytic efficiency.[45]

Another report from Liu *et al.*[163] reported the formation of 2D nanosheets by the sonication of SnS_2/*n*-propylamine in HNO_3 solution to exfoliate the bulk SnS_2 into SnS_2 nanosheets, as shown in Fig. 7(e). The exfoliation of inorganic (SnS_2)–organic hybrids that are composed of few- or single-layered inorganic targeting slabs sandwiched by a single-layer organic molecule *via* coordinated bonds. The inserting organic molecule can be removed by the ion exchange method. In this research, they also confirmed the improvement of the charge carrier lifetime investigated by photocurrent measurement compared with bulk materials as shown in Fig. 7(f). Moreover, the charge carrier lifetime was observed to be around 0.78 ns which is almost 10 times higher than bulk SnS_2. The Cr(VI) removal under visible light irradiation shows a significant improvement compared with bulk SnS_2 (Fig. 7(g)) with a degradation rate about 0.01436 min^{-1} which is 6 times higher than SnS_2 bulk materials. It indicates that the improvement of charge carrier separation from SnS_2 nanosheets has a direct correlation with the photocatalytic performance. Moreover, since SnS_2 nanosheets are a layered structure, the heterostructure of SnS_2 with other 2D materials was also interesting and has been explored by many researchers. For example, Zhang *et al.*[162] have prepared a 2D heterojunction SnS_2/MoS_2 photocatalyst for methylene blue degradation. In this work, they prepared two-step hydrothermal reactions, as shown in Fig. 7(h). At the initial stage the nanolayer of SnS_2 was prepared, and the MoS_2 layers grew on the SnS_2 surface using a hydrothermal reaction. The formation of a 2D heterostructure of SnS_2/MoS_2 nanosheets can increase the charge separation efficiency, which leads to an increase in the photocurrent signal, as shown in Fig. 7(i). The photocurrent density of SnS_2/MoS_2 was 15.20 mA cm^{-2} in the stable second cycle, which exhibited an 8.8 times enhancement compared with that of SnS_2 (~1.55 mA cm^{-2}) and a 23.1 times improvement com-

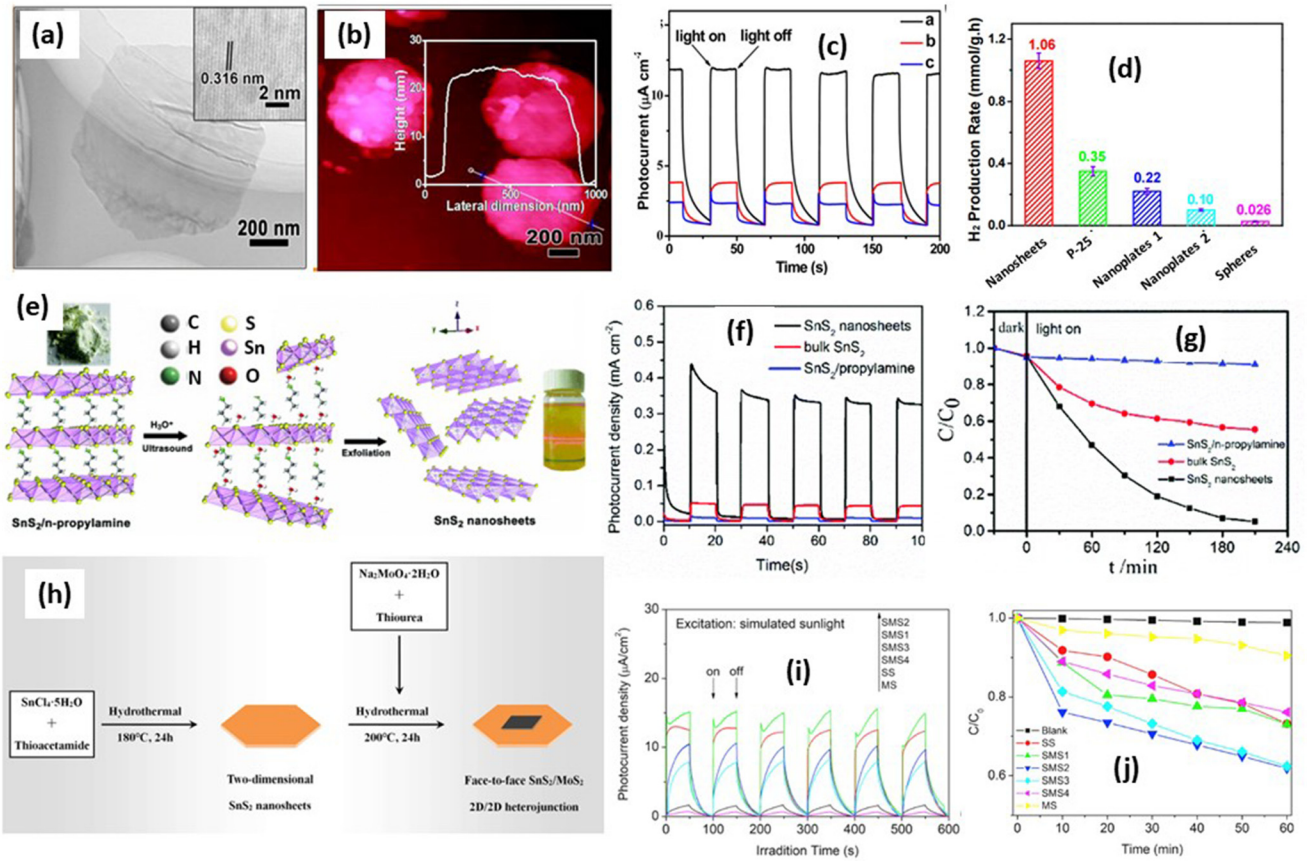

Fig. 7 (a) TEM image of an individual nanosheet. Inset is an HRTEM image. (b) High-magnification AFM image and corresponding height profile.[45] (c) The photoelectrochemical response of the samples at 0.8 V *versus* SCE electrode under 300 W Xe lamp illumination (λ > 420 nm). (Reproduced from ref. 45 with permission from the American Chemical Society, copyright 2014.) (d) Comparison of the photocatalytic hydrogen production rate of the samples. (e) Schematic illustration of the exfoliation of bulk SnS_2/*n*-propylamine into few-layer SnS_2 nanosheets. (f) Chronoamperometry at 0.6 V *vs.* Hg/Hg_2SO_4. (g) Photocatalytic reduction of 100 mg L^{-1} Cr(VI) with (1) the bulk SnS_2/*n*-propylamine hybrid, (2) bulk SnS_2, and (3) SnS_2 nanosheets.[163] (Reproduced from ref. 163 with permission from the Royal Society Chemistry, copyright 2019.) (h) A schematic drawing of the synthetic process of SnS_2/MoS_2. (i) Photocurrent and (j) photocatalytic activities of SS (SnS_2), SMS1 (SnS_2/MoS_2 (Mo : Sn = 1%)), SMS2 (SnS_2/MoS_2 (Mo : Sn = 2.5%)), SMS3 (SnS_2/MoS_2 (Mo : Sn = 5%)), SMS4 (SnS_2/MoS_2 (Mo : Sn = 75%)) and MS (MoS_2) for methylene blue decomposition under UV-vis irradiation.[162] (Reproduced from ref. 162 with permission from Elsevier, copyright 2019.)

pared with that of MoS_2 (~0.63 mA cm^{-2}). This phenomenon occurred due to the improvement of the charge separation efficiency due to the charge transfer between MoS_2 and SnS_2, which can prolong the charge carrier lifetimes. The photocatalytic activity is also directly correlated with the photocurrent result as shown in Fig. 7(j). The best sample SnS_2/MoS_2 demonstrated an enhanced photocatalytic rate of 81% compared with SnS_2.

3.2.3 Nanoparticles. Nanoparticles can be defined as particles with a diameter of less than 100 nm in size, offering numerous advantages over bulk-size materials, including an increased specific surface area, higher defect density, and improved dispersibility. Several reports have highlighted the photocatalytic performance of SnS_2 nanoparticles.[16,25,41,105,164–167] Fakhri *et al.*[41] reported the formation of SnS_2 nanoparticles by a hydrothermal reaction with the addition of 5 vol% acetic acid and 0.005 mol $SnCl_4·5H_2O$ and 0.02 mol thioacetamide. The produced nanoparticle was about 20–30 nm as shown in Fig. 8(a) and (b). They conducted a photocatalytic investigation for ENRO degradation under 500 W xenon irradiation, revealing a degradation rate of approximately 0.0296 min^{-1} using SnS_2 nanoparticles as catalyst (Fig. 8(c)).

Zhang *et al.*[105] conducted a more detailed investigation into SnS_2 nanoparticle formation and its photocatalytic ability. They controlled the particle diameter and specific surface area of the SnS_2 particle by adjusting parameters such as sulfur source concentration and reaction temperature during the hydrothermal process. Increasing the reaction temperature resulted in larger particle sizes, as depicted in Fig. 8(d) and (e). For instance, particles prepared at 180 °C had an average size of around 142 nm, while those from the 120 °C hydrothermal reaction were about 23 nm in size. Conversely, higher sulfur source concentrations led to smaller particle sizes, illustrated in Fig. 8(e) and (f). For instance, the particle size decreased to 46 nm when the sulfur source concentration was

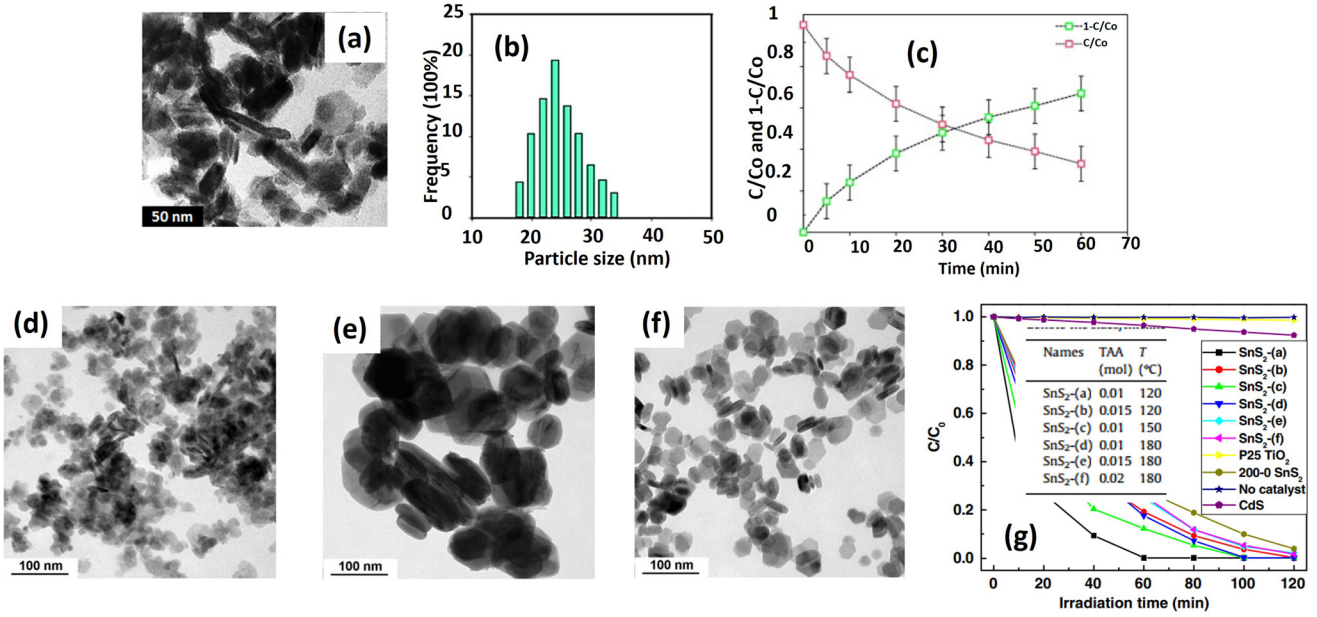

Fig. 8 (a) TEM image and (b) particle size distribution of SnS_2 NPs; (c) the photodegradation of ENRO by SnS_2 NPs under visible light.[41] (Reproduced from ref. 41 with permission from Elsevier, copyright 2015.) TEM images of SnS_2 prepared with (d) 0.01 mol of TAA at 120 °C; (e) 0.01 mol of TAA at 180 °C; and (f) 0.02 mol of TAA at 180 °C; (g) photocatalytic activities of SnS_2, flower-like CdS and P25 TiO_2 in degrading MO in distilled water under visible light (420 nm) irradiation.[105] (Reproduced from ref. 105 with permission from Elsevier, copyright 2011.)

increased from 0.01 mol to 0.02 mol. Higher reaction temperatures promote lower viscosity and enhance the diffusion of constituent Sn^{4+} and S^{2-} ions. Moreover, they accelerate Ostwald ripening rates, resulting in larger particle sizes.[105]

On the other hand, increasing the initial amount of thioacetamide from 0.01 to 0.02 mol releases more S^{2-} ions, saturating the reaction solution further. Consequently, a greater number of SnS_2 crystal nuclei form in the initial stages, reducing the available Sn^{4+} for subsequent crystal growth during the hydrothermal reaction and resulting in smaller particle sizes. Photocatalytic degradation of methyl orange reveals that SnS_2 synthesized at 120 °C exhibits superior performance compared with the sample prepared at 180 °C (Fig. 8(g)). The variation in particle size accounts for the observed differences, significantly influencing the available surface area and creating additional active sites to facilitate photocatalytic reactions. Furthermore, smaller particle sizes commonly lead to defect formation, serving as electron traps that prolong the lifetime of electrons and holes, thus promoting the photocatalytic degradation of methyl orange.

3.2.4 Quantum dots. Among other morphologies, quantum dots are one of the most unique morphologies regarding their physical properties. Quantum dots can be defined as particles of less than 10 nm. The uniqueness of these quantum dots is their properties, which are significantly affected by size, called the quantum size effect. Quantum dots are also recognized as having a high surface-to-volume ratio, which is comparable with larger two-dimensional nanosheets.[168] In the case of SnS_2, several reports have successfully synthesized SnS_2 quantum dots using various methods.[47,127,168–172] Zhao *et al.*[169] have reported the size-control of SnS_2 quantum dots using the sonication method with PEG400 as a solvent. They controlled the quantum dot size by varying the heating times after the sonication process. Fig. 9(a–d) shows the TEM images of SnS_2 quantum dots prepared by different heating times of 4, 8, 12, and 16 h, respectively. The particle size distribution of each sample plotted in the inset of each figure indicates the increase in the size with the increase of heating time from 5 to 10 nm.

Interestingly, the UV-Vis absorbance of SnS_2 quantum dots largely shifted to the larger wavelength, indicating the narrower band gap value after increasing the particle size (Fig. 9(e)). This behavior is a typical characteristic of quantum dot particles where the band gap energy is greatly affected by size. Quantum-sized particles have a higher surface area-to-volume ratio, which increases the probability of photon absorption; moreover, quantum-sized particles often exhibit higher charge carrier mobility due to their unique electronic structure and reduced dimensionality. Enhanced mobility facilitates the efficient separation and migration of photogenerated electron–hole pairs, which are essential for driving redox reactions in photocatalysis. The luminescence analysis (Fig. 9(f)) has also confirmed the emission shift because of electron excitation. The significant shift in the band gap with a slight increase in size is one of the unique features of quantum dots due to the quantum confinement effect, which is beneficial for luminescence applications. On the other hand, Wang *et al.*[173] reported the fabrication of a Si-photoanode incorporating SnS_2 quantum dots for the hydrogen evolution reaction. In Fig. 9(g), the TEM image displays the par-

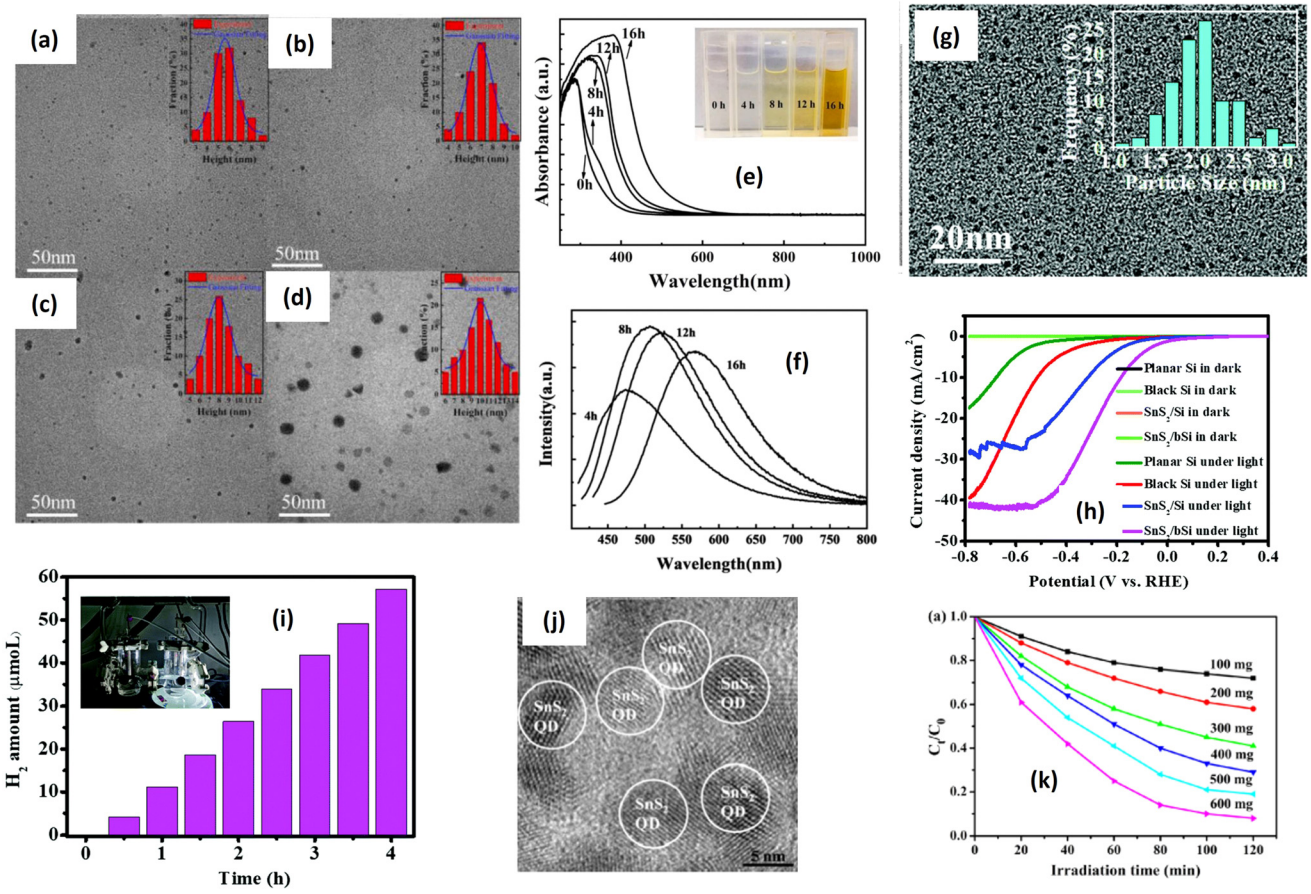

Fig. 9 TEM (inset: size distribution) images of SnS_2 QDs after heating for (a) 4 h; (b) 8 h; (c) 12 h; and (d) 16 h. (e) Absorption spectra of SnS_2 QDs with different heating times. (f) Luminescence analysis of SnS_2 QDs with different heating times.[169] (Reproduced from ref. 169 with permission from Elsevier, copyright 2023.) (g) TEM images of as-synthesized SnS_2 QDs. (h) Lateral size distribution of SnS_2 QDs;[173] (reproduced from ref. 173 with permission from the Royal Society of Chemistry, copyright 2019). (i) The calculated photocurrent density under various wavelengths; (j) HR-TEM images of SnS_2 QDs; (k) effect of the dosage of the SnS_2 QD photocatalyst on the photocatalytic reduction of 100 mg L^{-1} Cr(VI) under visible-light irradiation (λ = 420 nm).[47] (Reproduced from ref. 47 with permission from Elsevier, copyright 2016.)

ticle distribution of SnS_2 quantum dots, with an average size of approximately 2 nm. Fig. 9(h) illustrates the polarization curves of planar Si, SnS_2/pSi, black Si, and SnS_2/bSi samples. All the Si electrodes exhibit noticeable current responses under illumination, contrasting with dark conditions. Additionally, the SnS_2/bSi photocathode demonstrates a maximum photocurrent of ~41 mA cm^{-2} at approximately −0.51 V, attributed to the light-harvesting nanostructure of black Si and the active sites of the SnS_2 catalyst. The hydrogen evolution reaction (Fig. 9(i)) indicates a hydrogen amount of about 55 μmol L^{-1} after irradiation. The photocatalytic performance of SnS_2 quantum dots has been also reported by Tu *et al.*[47] for Cr(VI) reduction under visible light irradiation. The quantum size SnS_2 has been successfully prepared for hydrothermal reaction with L-cystine as a particle-controlling agent. SnS_2 quantum dots with a size of 6.32 nm have been obtained, as shown in Fig. 9(j). The photocatalytic performance of SnS_2 quantum dots also shows good potential for wastewater treatment (Fig. 9(k)). Comparing various morphologies, it is anticipated that the most suitable morphology for photocatalytic applications can be identified. Different morphologies can be achieved by adjusting several parameters during the synthesis process. As shown in Table 3, diverse morphologies, including flower-like structures, nanolayers, nanoparticles, and quantum dots, have been synthesized using different methods. Upon evaluating the apparent rate constants derived from the catalytic activities, it becomes evident that the flower-like structure exhibits the most effective photocatalytic reaction, with a degradation rate of approximately 0.0692 min^{-1}, followed by the nanoparticle morphology with the highest observed degradation rate of about 0.0594 min^{-1}. The superior photocatalytic performance of the flower-like morphology is attributed to its large specific surface area, excellent interfacial contact, and rapid electron transfer.[157] The enhanced photocatalytic properties of the flower-like structure can be elucidated as follows: the abundant petal-like structures provide more surface area for photochemical reactions to occur upon irradiation and interaction with chemicals, while the arrangement of flower-like structures traps light, thereby increasing electron–hole generation.[174] Furthermore, the open and porous nature of

Table 3 Photocatalytic activities of morphologically modified SnS_2

Morphology type	Light source	Synthesis method	Photocatalytic testing	Photocatalytic result	Ref.
SnS_2-flower-like	300 W xenon lamp	Hydrothermal (at 180 °C, 9 h) 80 mL 0.01 M $SnCl_4{\cdot}5H_2O$ and L-cysteine	100 mg L^{-1} rhodamine B degradation	Degradation rate: 0.0251 min^{-1}	50
SnS_2 flower-like	300 W xenon lamp	Solvothermal in ethanol, (180 °C, 12 h) 2 mmol $SnCl_4{\cdot}5H_2O$ and 5 mmol CH_3CSNH_2 (thioacetamide)	10 ppm rhodamine B degradation	Degradation rate: 0.0692 min^{-1}	36
SnS_2 flower-like	400 W metal halide lamp	Hydrothermal (200 °C, 24 h) 10 mmol $SnCl_4{\cdot}5H_2O$, and 3.04 g (40 mmol) thiourea	10 ppm methylene blue degradation	Degradation rate: 0.0179 min^{-1}	176
SnS_2 flower-like	300 W xenon lamp	Hydrothermal (180 °C, 3 days) 100.0 mg SnO_2 hollow multi-shelled microspheres and 1.0 g thioacetamide	CO_2 reduction	CO production rate 8.91 μmol g^{-1} h^{-1}	135
SnS_2-nanosheets	300 W xenon lamp	Solvothermal in ethanol with acetic acid (180 °C, 12 h) 0.25 mmol $SnCl_4{\cdot}5H_2O$, 0.625 mmol of thioacetamide	Nitrogen fixation	NH_4^+ yield: 27.5 μmol g^{-1} h^{-1}	101
SnS_2-nanosheets	300 W xenon lamp	Sonication in an ice-water bath for 1 h	50 mg L^{-1} Cr(VI) reduction	$k_{Cr(VI)}$ = 0.01436 min^{-1}	163
SnS_2-nanosheets	300 W xenon lamp 320 nm filter	Solvothermal in triethylene glycol (220 °C, 12 h). 1 mmol $SnCl_2{\cdot}2H_2O$, 2 mmol TAA and 0.5 g PVP	Hydrogen generation	H_2 production rate: 1.06 mmol g^{-1} h^{-1}	45
SnS_2-nanosheets	400 W mercury lamp	Hydrothermal with ethylenediamine (200 °C, 24 h). 3.5 g (10 mmol) of stannic(IV) chloride and 3.04 g (40 mmol) of thiourea	Hydrogen generation	H_2 production rate: 0.566 mmol g^{-1} h^{-1}	31
SnS_2-nanosheets	400 W mercury lamp	Hydrothermal with ethylenediamine (200 °C, 24 h). 3.5 g (10 mmol) of stannic(IV) chloride and 3.04 g (40 mmol) of thiourea	Methylene blue degradation	k_{MB}: 0.0178 min^{-1}	31
SnS_2-nanoparticle	250 W xenon lamp 420 nm filter	Hydrothermal (130–170 °C). 5 mmol $SnCl_4{\cdot}5H_2O$, 10 mmol thioacetamide	50 mg L^{-1} Cr(VI) reduction	$k_{Cr(VI)}$: 0.0394 min^{-1}	164
SnS_2-nanoparticle	250 W xenon lamp 420 nm filter	Hydrothermal (140–180 °C). 5 mmol $SnCl_4{\cdot}5H_2O$, 10 mmol thioacetamide	20 mg L^{-1} methyl orange degradation	k_{MO}: 0.0594 min^{-1}	105
SnS_2-nanoparticle	500 W xenon lamp	Hydrothermal + acetic acid (130–170 °C, 12 h). 0.005 mol $SnCl_4{\cdot}5H_2O$ and 0.01–0.02 mol thioacetamide	10 mL of log phase culture's antibacterial reaction	The bacteria killing ability of 0.11 g mL^{-1} NPs: 75.28 ± 2.3% for *S. aureus* (ATCC 25923), 78.95 ± 2.0% for *E. coli* (ATCC 13534), 81.22 ± 1.1% for *E. coli* (ATCC 25922)	41
SnS_2 quantum dots	300 W Xe lamp equipped with a cut-off filter (λ > 420 nm)	Hydrothermal at (160 °C, 16 h) Sn source: $SnCl_4{\cdot}5H_2O$ S source: L-cystine modifier	100 mg L^{-1} of Cr(VI) reduction	Degradation ability: 92% for 2 h	47

flower-like structures facilitates a better mass transfer of reactants and products,[175] enhancing accessibility to active sites and promoting more effective contact between the photocatalyst and target pollutants in the surrounding environment.

3.3 Heterostructure formation

Heterostructure photocatalysts have garnered widespread acceptance as a highly promising technique for the development of high-performance photocatalysts. The heterostructures can be defined as the combination of photocatalysts with other materials (other photocatalysts or co-catalysts). The key advantage of heterostructure formation lies in the synergistic effects between the different materials, wherein each component mutually reinforces the other, thereby enhancing the overall photocatalytic performance.[177,178] As illustrated in Fig. 3(b), the current literature demonstrates that approximately 75% of published works on SnS_2-based photocatalysts involve heterostructure formation. Diverse materials, including semiconductors, metals, and 2D materials such as graphene and its derivatives, have been combined with SnS_2 and exhibit a significant impact on the photocatalytic properties, such as the improvement of specific surface area, heightened light sensitivity, and enhanced reactivity. Furthermore, a crucial aspect is its ability to mitigate the recombination of electrons and holes through the formation of heterojunctions. A heterojunction is an electrical transfer between two or more materials resulting from differing electronic states and band positions. This phenomenon extends the lifetimes of electrons and holes, providing them with more time to promote redox reactions for photocatalytic reactions. To date, various types of heterojunction formation exhibit distinct characteristics and effects on photocatalytic reactions, including type I, type II, p–

n junction, Schottky junction, and Z-scheme, as illustrated in Fig. 10.[179]

3.3.1 Schottky junction and surface plasmon resonance. A Schottky junction typically forms during the interaction between a metal and a semiconductor. Upon contact, electrons from the semiconductor tend to flow towards the metal until a Fermi equilibrium is reached. Subsequently, a barrier potential arises, hindering the further flow of electrons into the metal unless they overcome this potential barrier. The Schottky barrier effectively acts as an electron trap, preventing the electrons from flowing back into the semiconductor. This characteristic turns the metal into an electron sink for the photoinduced electrons. The Schottky barrier serves to impede the recombination of electron–hole pairs, thereby extending the lifespan of electrons for the photoreaction.[180]

The exploration of Schottky junction processes in SnS_2 photocatalysts remains limited in the existing literature, with only a few reports delving into this phenomenon with different types of noble metal including Pt,[37] Au,[181] and Ag.[182] Among other noble metals, gold (Au) has emerged as one of the extensively studied supports for SnS_2 photocatalysts. Feng *et al.*[183] reported the deposition of Au on SnS_2 nanoflowers prepared *via* hydrothermal synthesis for methylene blue degradation under visible light irradiation. The transmission electron microscopy (TEM) images in Fig. 11(a and b) reveal a 20 nm size of Au deposition on 3 μm size SnS_2 nanoflowers, indicating intimate contact between the Au and SnS_2, which enhances the charge transfer efficiency. Fig. 11(c) demonstrates the methylene blue degradation ability of Au-deposited SnS_2 with varying Au concentrations, showcasing a significant enhancement in degradation after Au deposition. Specifically, the degradation rate of Au–SnS_2 was approximately 3.91 times higher than that of SnS_2 nanoflowers alone (Table 4). The pronounced improvement in methylene blue degradation post-Au deposition can be attributed to the enhanced charge carrier efficiency facilitated by the Schottky junction formation between Au and SnS_2 (Fig. 11(d)). As the Fermi level of Au is lower than that of SnS_2, electron transfer from SnS_2 to Au occurs, effectively preventing electron–hole recombination. This allows the generation of radicals necessary for methylene blue molecule dissociation. Charge separation efficiency, typically reflected in the number of mobile electrons on the surface, was assessed through photocurrent measurement (Fig. 11(e)). Mondal *et al.*[184] endeavored to decompose benzylamine using Au–SnS_2 nanosheets under solar irradiation. Synthesized *via* a hydrothermal reaction followed by gold photoreduction using a 400 W xenon lamp, Au-deposited SnS_2 nanosheets achieved a conversion rate of approximately 98%

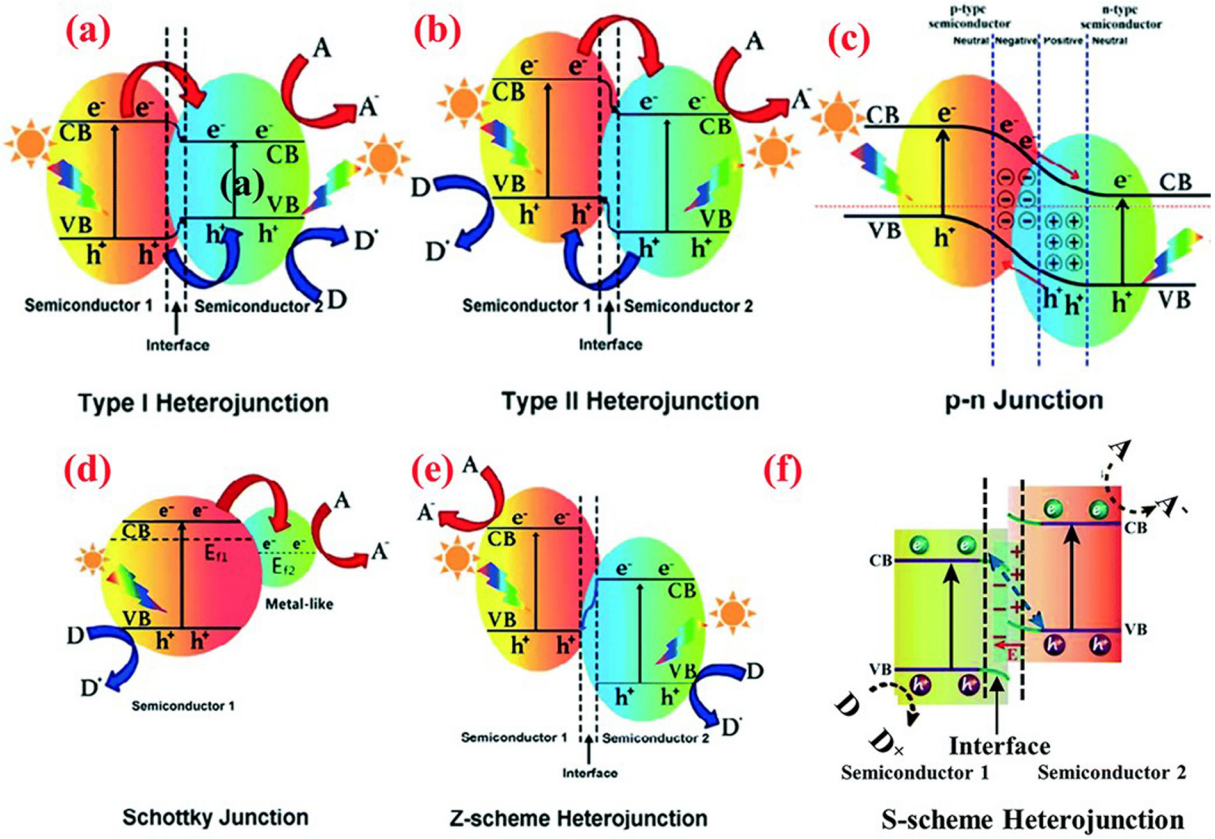

Fig. 10 Band structure of various types of heterojunction in a photocatalytic hybrid nanocomposite: (a) type I heterojunction; (b) type II heterojunction; (c) p–n junction; (d) Schottky junction; (e) Z-scheme heterojunction; and (f) S-scheme heterojunction.[179] (Reproduced from ref. 179 with permission from the Royal Society of Chemistry, copyright 2021.)

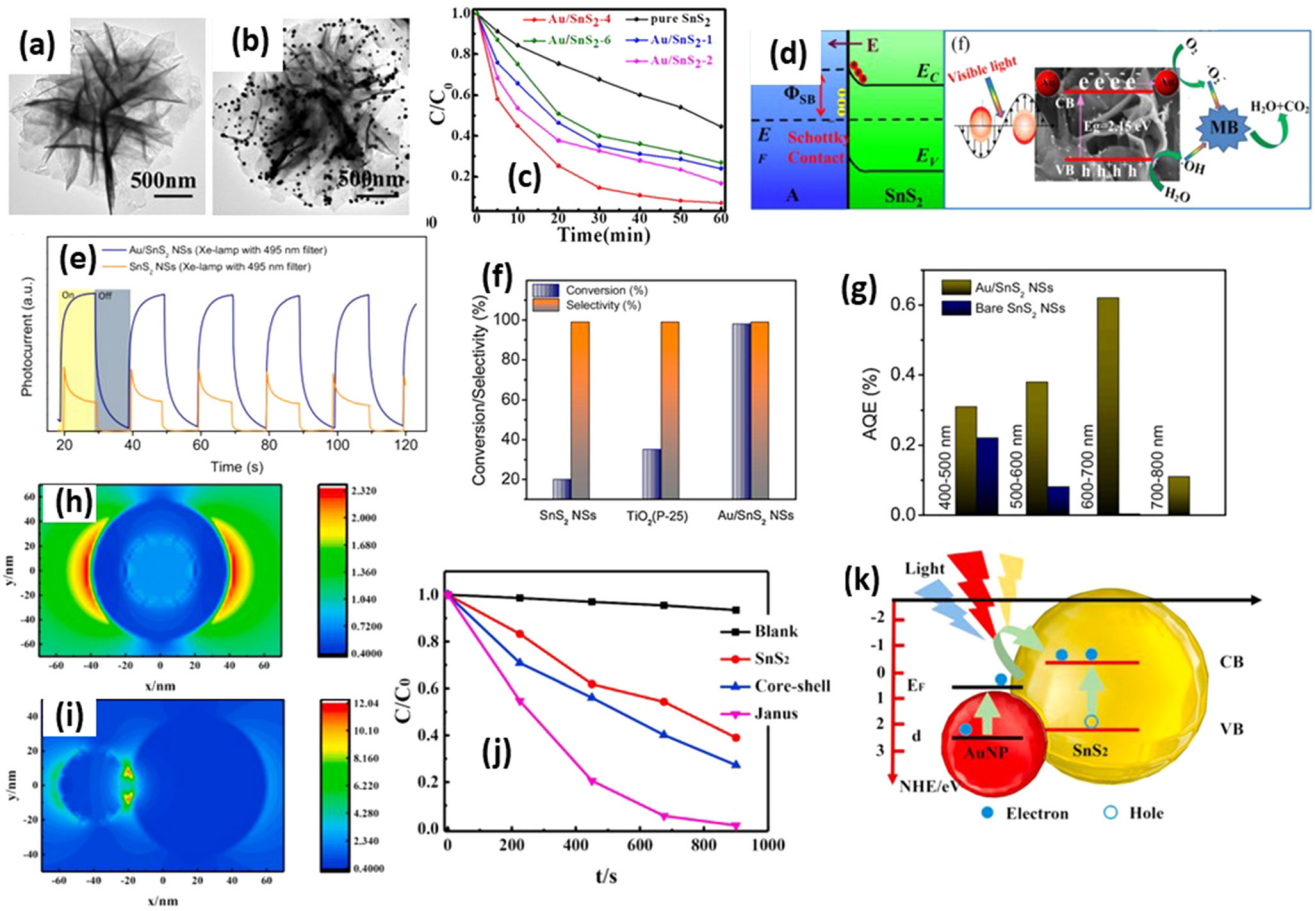

Fig. 11 TEM images of (a) SnS_2 and (b) Au/SnS_2. (c) Methylene blue degradation by Au/SnS_2. (d) Illustration of the band alignment formed at the interface between the SnS_2 and Au NPs.[183] (Reproduced from ref. 183 with permission from Elsevier, copyright 2019.) (e) Transient photocurrent recorded on bare SnS_2 and Au/SnS_2 NSs using a 400 W Xe lamp (with an attached 495 nm cut-off filter). (f) Comparison plots of benzylamine oxidation efficiency with different catalysts under natural sunlight and ambient conditions for 2 h in open air. (g) Plot of AQE at different wavelength ranges under LED illumination in air at room temperature for bare SnS_2 and Au/SnS_2.[184] (Reproduced from ref. 184 with permission from Elsevier, copyright 2021.) (h) The near-field distribution of the core–shell structure and the (i) Janus structure with Au nanoparticle s, respectively. (j) Degradation curves of methyl orange under visible light. (k) The schematic diagram of the LSPR-enhanced visible light catalysis of SnS_2 and the heterostructures with Au nanoparticles.[186] (Reproduced from ref. 186 with permission from Elsevier, copyright 2021.)

under solar light (Fig. 11(f)), surpassing SnS_2 and standard P-25 conversion rates of about 20% and 35%, respectively (Table 4).

To investigate the photocatalytic enhancement in Au–SnS_2 nanosheets, the apparent quantum efficiency (AQE) was examined at different wavelengths (400–500 nm, 500–600 nm, 600–700 nm, 700–800 nm) (Fig. 11(g)). Compared with SnS_2 nanosheets, Au–SnS_2 exhibited a 1.2 to 3 times higher AQE at 400–500 nm and 500–600 nm wavelengths, attributed to improved electron–hole separation mediated by Au nanoparticles (Fig. 11(g)). Notably, at 600–700 nm, where SnS_2 excitation is minimal, Au-deposited SnS_2 exhibited a strong AQE, indicating an efficient 'hot-electron' injection mechanism from Au nanoparticles to SnS_2 nanosheets.[185] Furthermore, the formation of Au–SnS_2 is influenced by Au positioning relative to the SnS_2 photocatalyst. Fu *et al.*[186] investigated different composite structures of Au–SnS_2 for methyl orange degradation under visible light. Two structures were examined: core–shell and Janus structures. Near-field distribution analysis (Fig. 11(h and i)) revealed a low light enhancement effect in the core–shell structures, leading to diminished photocatalytic ability. Conversely, Janus structures exhibited a significant near-field enhancement, resulting in superior methyl orange degradation (Fig. 11(j)). Among the images, the Janus structures exhibit the highest reaction rate (4.0×10^{-3} s^{-1}), followed by the core–shell structures (1.2×10^{-3} s^{-1}). A significant increase in photocatalytic activity, approximately four times greater than that of sole SnS_2 nanoparticles (1.0×10^{-3} s^{-1}), is observed in the Janus structures. This enhancement is attributed to the improved extinction effect. Photoluminescence lifetime analysis revealed longer electron lifetimes in nanoparticle structures (1.74 ns) than Janus structures (1.53 ns) compared with core–shell structures (1.16 ns), indicating an enhanced photocatalytic efficiency. Fig. 11(k) illustrates the proposed

Table 4 Photocatalytic performance of heterojunction formation of SnS_2

Materials	Heterojunction type	Light source	Photocatalytic testing	Photocatalytic performance	Ref.
Au–SnS_2	Schottky junction	330 W xenon lamp	100 mg L^{-1} rhodamine B degradation	k_{RhB}: 0.0514 min^{-1}. 3.91 times that of SnS_2	183
Au–SnS_2	Schottky junction	400 W xenon lamp	Benzylamine oxidation	Conversion: 98%, 4.9 times that of SnS_2	184
Au–SnS_2	Schottky junction	250 W xenon lamp	50 mg L^{-1} Cr(VI) reduction	$k_{Cr(VI)}$: 0.0234 min^{-1}. 2.07 times that of SnS_2	73
$BiFeO_3$/SnS_2	p–n junction	250 W mercury lamp	15 mg L^{-1} methylene blue degradation	k_{MB}: 0.0428 min^{-1}. 7.50 times that of SnS_2	188
BiOI/SnS_2	p–n junction	UV-vis (385–740 nm)	10 mg L^{-1} rhodamine B degradation	k_{RhB} 100% within 30 min 3 times that of SnS_2	187
TiO_2/SnS_2	Type I heterojunction	Xe lamp, 100 mW cm^{-2}	Hydrogen evolution reaction (HER)	H_2 yield: 652.4 μmol g^{-1} h^{-1} 7.51 times that of SnS_2	190
$ZnIn_2S_4$/SnS_2	Type II heterojunction	300 W xenon lamp	50 mg L^{-1} Cr(VI) reduction	$k_{Cr(VI)}$: 0.01273 min^{-1} 2.2 times that of SnS_2	196
$ZnWO_4$/SnS_2	Type II heterojunction	Solar hotspot 5 kW h m^{-2} day^{-1}	50 mg L^{-1} Cr(VI) reduction	$k_{Cr(VI)}$ = 0.061 min^{-1} 3.58 times that of SnS_2	104
$ZnWO_4$/SnS_2	Type II heterojunction	Solar hotspot 5 kW h m^{-2} day^{-1}	20 mg L^{-1} tetracycline	k_{TC} = degradation rate: 0.023 min^{-1} 3.28 times that of SnS_2	104
In_2S_3/SnS_2	Type II heterojunction	300 W xenon lamp	10 mg L^{-1} rhodamine B degradation	k_{RhB}: 0.11716 min^{-1}. 15.3 times that of SnS_2	192
Ag_3PO_4/SnS_2	Z-scheme	A 500 W xenon-arc lamp	10 mg L^{-1} methylene blue	k_{MB} = 0.063 min^{-1} 7.08 times that of SnS_2	201
Bi_2WO_4/SnS_2	Z-scheme	Sunlight	20 mg L^{-1} tetracycline degradation	k_{TC} = 0.027 min^{-1} 27 times that of SnS_2	134
BiOBr/SnS_2	Z-scheme	400 W xenon lamp	10 mg L^{-1} rhodamine B degradation	k_{RhB} = 0.1203 min^{-1} 75 times that of SnS_2	197
SnO_2/SnS_2	S-scheme	500 W xenon lamp	10 mg L^{-1} methyl orange degradation	k_{MO}: 0.01182 min^{-1}. 2.19 times that of SnS_2	199
$ZnIn_2S_4$/SnS_2	S-scheme	300 W xenon lamp	H_2 production	H_2 yield: 1.113 mmol g^{-1} h^{-1} 16.14 times that of $ZnIn_2S_4$	200
CdS/SnS_2	S-scheme	300 W xenon lamp	H_2 production	H_2 yield: 5.18 mmol g^{-1} h^{-1} 5.95 times that of CdS	198

mechanism of surface resonance analysis of Janus Au–SnS_2; due to the near-field enhancement, electron excitation becomes more pronounced in SnS_2 nanoparticles, significantly enhancing photocatalysis. Besides the enhanced optical fields, the localized surface plasmon resonance (LSPR) induces electron injection from AuNPs to the conduction band edge of SnS_2, further contributing to the photocatalytic process. Among these mechanisms, the excited electrons in the conduction band edge of the SnS_2 nanoparticles facilitate the generation of reactive oxygen radicals, including superoxide, hydroxyl, and singlet oxygen, through a series of oxidation–reduction processes in the solution. These oxygen radicals exhibit high activity and play a crucial role in degrading methyl orange molecules.[186]

3.3.2 p–n junction. The p–n junction arises from electronic interactions driven by differences in the majority carriers of semiconductors. In n-type semiconductors, electrons predominate as majority carriers, whereas in p-type semiconductors, holes are prevalent. Electrons flow from n-type to p-type, while holes migrate oppositely, impeding electron–hole recombination. SnS_2, an n-type semiconductor, is frequently combined with various p-type semiconductors like as BiOI,[187] $BiFeO_3$,[188] NiS,[189] and SnS nanoparticles[16] to create p–n junction photocatalysts.

Wang *et al.*[187] confirmed the p–n junction formation between BiOI and SnS_2 for rhodamine B degradation under visible light irradiation, as illustrated in Fig. 12(a). Notably, SnS_2 has a layered morphology, while BiOI comprises the nanoparticles that disperse on the top of the SnS_2 layer. The conduction band of SnS_2 is situated at −0.96 V, with a valence band at 1.5 V. Conversely, BiOI exhibits a valence band at +0.53 V and a conduction band at −1.29 V. Upon electrical contact, band alignment ensues, facilitating electron and hole transfer between the BiOI and SnS_2 until equilibrium is attained, with the Fermi level equalized. Upon irradiation, electron–hole pairs form in the conduction and valence bands of SnS_2 and BiOI. Due to the p–n junction, electrons readily transfer from BiOI to SnS_2, while holes undergo the reverse process. This reaction process enhances electron mobility and correlates directly with photocatalytic efficiency. Photocurrent analysis (Fig. 12(b)) demonstrates increased electron densities of BiOI/SnS_2 heterostructures compared with BiOI and SnS_2. The active electrons in the conduction band react with O_2 to form $O_2^{\bullet-}$, while the holes react with OH^- to produce $OH^{\bullet}$, facilitating rhodamine B degradation. Rhodamine B degradation analysis (Fig. 12(c)) indicates a significant improvement after p–n junction formation, three times higher than that observed with SnS_2 alone (Table 4), a finding consistent with the photocurrent analysis.

3.3.3 Type I and II heterojunctions. Fig. 13(a) illustrates a type I heterojunction within a photocatalytic reaction. Type I heterojunctions manifest when a semiconductor with a rela-

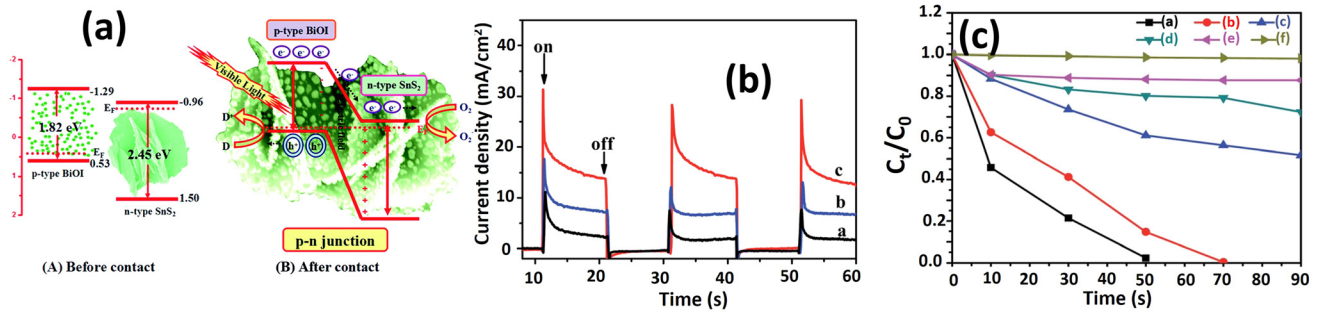

Fig. 12 (a) Schematic diagrams illustrating the energy bands of p-BiOI and n-SnS_2 before contact, the formation of a p–n junction, and the equilibrium energy band diagram. Additionally, the transfer of photoinduced electrons from p-BiOI to n-SnS_2 under visible-light irradiation is depicted; (b) comparison of the transient photocurrent response of SnS_2 (black), BiOI (blue), and BiOI/SnS_2 (red) in 0.1 M Na_2SO_4 aqueous solution under visible-light irradiation; (c) visible-light photocatalytic activities: (black) BiOI/SnS_2, (red) BiOI, (blue) SnS_2, (green) P25, (violet) adsorption in the dark, and (yellow) degradation of 10 mg rhodamine B without photocatalyst under visible light (λ > 420 nm) irradiation.[187] (Reproduced from ref. 187 with permission from the Royal Society of Chemistry, copyright 2015.)

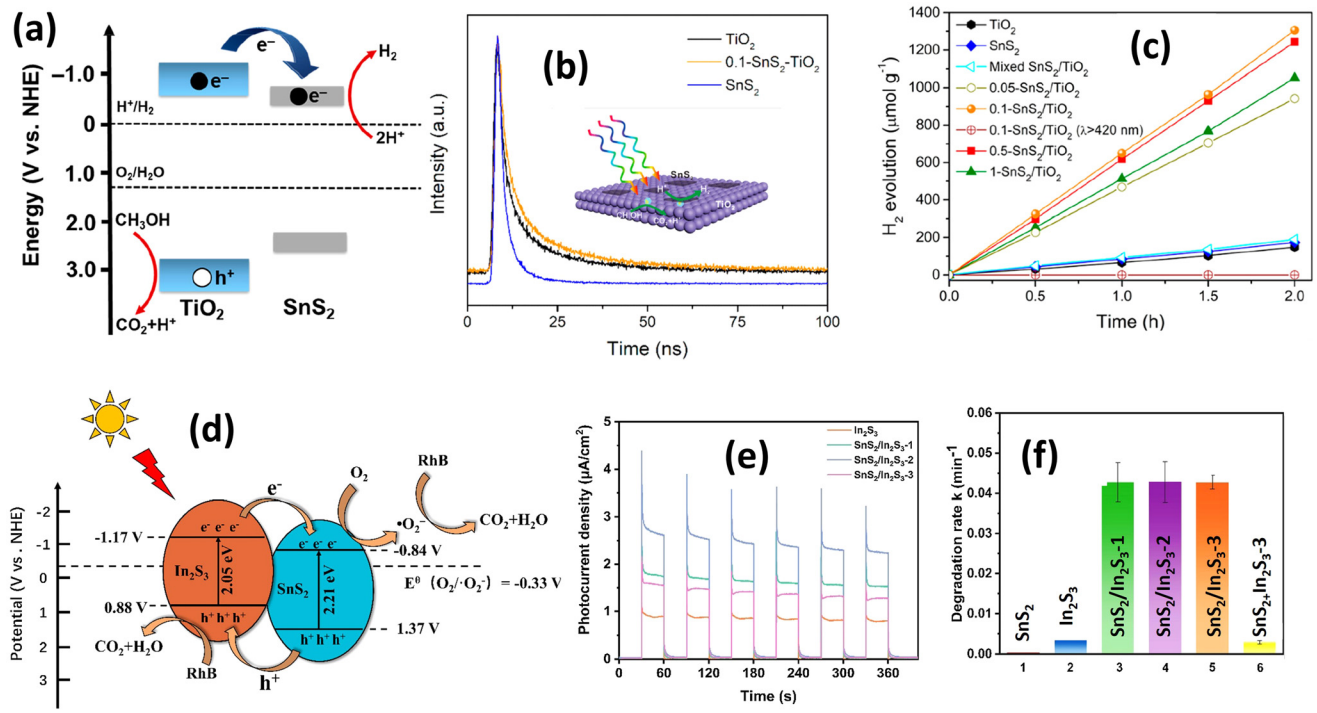

Fig. 13 (a) Corresponding band energy diagrams and charge transfer path; (b) time-resolved photoluminescence decay spectra of TiO_2, SnS_2, and 0.1-SnS_2/TiO_2; (c) photocatalytic H_2 evolution curves with different catalysts.[190] (Reproduced from ref. 190 with permission from Elsevier, copyright 2019.) (d) Schematic diagram of the possible photocatalytic degradation mechanism of RhB by the SnS_2/In_2S_3 heterostructure under visible light irradiation; (e) transient photocurrent responses of In_2S_3 and SnS_2/In_2S_3 heterostructures; (f) the apparent rate constants of SnS_2/In_2S_3.[192] (Reproduced from ref. 192 with permission from Elsevier, copyright 2022.)

tively large band gap energy, such as TiO_2, interfaces with another semiconductor possessing a smaller band gap energy. The valence band and conduction band positions are intermediary between those of materials with larger band gaps. In this context, following photoexcitation, electrons and holes migrate from the large band gap photocatalyst to the smaller band gap photocatalyst, thereby facilitating reduction–oxidation reactions crucial for photocatalytic processes. Sun *et al.*[190] provide an exemplar of a type I heterojunction with a SnS_2 photocatalyst, detailing the formation of SnS_2/TiO_2 heterostructures. Fig. 13(a) elucidates the catalytic reaction process of type I heterojunction formation between SnS_2 and TiO_2. Under these reaction conditions, they propose that photoelectrons from the conduction band of TiO_2 migrate into the conduction band, reducing H^+ ions into hydrogen gas. Meanwhile, holes react with methanol to yield hydrogen gas. This heterojunction reaction prolongs the decay time of electrons, estimated at around 4.4 ns compared with TiO_2 (2.8 ns)

and SnS_2 (1.8 ns) as shown in Fig. 13(b). The hydrogen evolution reaction, as depicted in Fig. 13(c), showcased a remarkable enhancement facilitated by the 0.1-SnS_2/TiO_2 compared with SnS_2 and TiO_2 individually. The 0.1-SnS_2/TiO_2 nanohybrid exhibited an impressive hydrogen production rate, reaching 652.4 μmol h^{-1} g^{-1}, surpassing the rates observed with pure TiO_2 and SnS_2 by approximately 8 times. However, a further increase in the amount of SnS_2 in the hybrid resulted in a slight decline in H_2 production activity, with values of 621.5 and 526.7 μmol h^{-1} g^{-1} for 0.5-SnS_2/TiO_2 and 1-SnS_2/TiO_2, respectively. This phenomenon can be attributed to the excess SnS_2 hindering the absorption of incident light and the generation of excited carriers by TiO_2. Additionally, an abundance of SnS_2 may act as charge recombination centers, leading to a reduced photocatalytic performance. Another type I heterojunction formation has been reported by Liu *et al.*[191] investigating the formation of SnS/SnS_2 for the electrochemical water splitting process. They found that the energy gap of SnS_2 is 2.15 eV, while SnS has an energy gap of 1.1 eV. The conduction band (CB) and valence band (VB) positions of SnS_2 are −0.08 eV and 2.08 eV, respectively, whereas those of SnS are 0.12 eV and 1.22 eV, respectively. Given that the VB of SnS_2 is more positive while the CB is more negative, electrons and holes tend to migrate to SnS after electron excitation, effectively retarding electron and hole recombination. The photocurrent analysis revealed that the current density under irradiation for the SnS_2/SnS heterojunction is five times higher than that of SnS and ten times higher than that of SnS_2, confirming the charge carrier efficiency.

Differing from type I heterojunctions, type II heterojunctions involve semiconductor photocatalysts where two types of semiconductor exhibit distinct band structure levels. One semiconductor possesses a more positive valence band, while the other semiconductor has a more negative conduction band. In this arrangement, electrons flow from the semiconductor with the more negative conduction band position, while holes flow from the semiconductor with the more positive valence band. This electrical transfer scheme helps prevent electron and hole recombination. An example of a type II heterojunction formation of SnS_2 was reported by Zhang *et al.*[192] investigating the formation of SnS_2 with In_2S_3. Fig. 13(d) illustrates the catalytic reaction mechanism of the SnS_2/In_2S_3 heterostructure for rhodamine B degradation under visible light irradiation. Upon irradiation, electron transfer occurs from the conduction band of In_2S_3 to the conduction band of SnS_2 due to the more negative level of the conduction band position of In_2S_3, while hole transfer operates oppositely due to the greater positivity of the valence band level of SnS_2. Similar to a heterojunction type I, this charge transfer process between In_2S_3 and SnS_2 significantly enhances charge mobility efficiency, as demonstrated in Fig. 13(e); the photocurrent of the In_2S_3/SnS_2 heterostructure is 3–4 times higher than In_2S_3 only, which shows a marked improvement in current density after heterojunction formation. RhB degradation testing indicates a significant enhancement in RhB degradation by conducting In_2S_3/SnS_2 heterojunction formation (Fig. 13(f)), where the degradation rate was 99 times and 15 times higher than with SnS_2 and In_2S_3 alone, respectively. The theoretical explanation of the In_2S_3/SnS_2 heterojunction as type II heterojunction formation was confirmed by Wang *et al.*[193] through EPR analysis for detecting superoxide radicals. The lower intensity of the EPR signal of In_2S_3/SnS_2 compared with In_2S_3 indicates electron transfer from In_2S_3 to SnS_2, confirming type II heterojunction formation. Other materials have also formed type II heterojunctions combined with SnS_2, such as g-C_3N_4,[194] $ZnWO_4$,[104] SnO_2,[195] and $ZnIn_2S_4$.[196]

3.3.4 Z-scheme and S-scheme photocatalyst. However, based on above existing heterostructure systems there is still an issue regarding the reducing of the oxidation and reduction ability of the photocatalyst. To address this issue, scientists have pioneered the development of Z-scheme and S-scheme photocatalysts. These novel configurations offer superior reduction and oxidation capabilities compared with conventional type I and type II heterojunction formations. To date, Z-scheme and S-scheme heterojunctions have emerged as the most investigated heterostructures for SnS_2-based photocatalysts. Notably, the direct Z-scheme photocatalyst for SnS_2 holds considerable promise for future advancements, as it obviates the need for a metal mediator to facilitate Z-scheme reactions.

Several studies have confirmed the formation of direct Z-scheme photocatalysts. For instance, Luo *et al.*[15] initiated Z-scheme formation by integrating SnS_2 with Ag_3PO_4 for methyl orange degradation under visible light irradiation. The schematic representation in Fig. 14(a) illustrates the Z-scheme formation of the SnS_2/Ag_3PO_4 heterostructure. The realization of a direct Z-scheme photocatalyst depends on the band positions of each constituent material. In the case of the SnS_2/Ag_3O_4 heterostructure, the Z-scheme configuration is inferred from the disparate band positions of the SnS_2 and Ag_3PO_4.

The formation of a direct Z-scheme photocatalyst relies on the band positions of each material. In the case of the SnS_2/Ag_3PO_4 heterostructure, the existence of the Z-scheme can be inferred from the disparate band positions of each material. The valence band (VB) maximum and conduction band (CB) minimum of SnS_2 are about 1.21 eV and −0.89 eV, respectively, while the VB and CB potentials of Ag_3PO_4 are about 2.62 eV and 0.30 eV, respectively. The CB position of Ag_3PO_4 is more positive than the standard reduction potential of $O_2/O_2^{\bullet-}$ (0.13 eV). The electron from Ag_3PO_4 is unable to reduce O_2 into $O_2^{\bullet-}$ and instead reacts with the hole of the SnS_2. Consequently, recombination is prevented, leading to a more efficient charge separation process, as demonstrated by photocurrent analysis. This correlation directly corresponds to the observed improvements in photocatalytic activity (see Fig. 14(b and c)). As mentioned earlier, the Z-scheme can be generated if one of the conduction bands (CBs) of the sample position is more positive than the reduction potential of $O_2/O_2^{\bullet-}$ (0.13 eV), thereby preventing the reduction reaction. Other reports also confirm the same understanding about the Z-scheme formation, such as Qiu *et al.*,[197] Li *et al.*,[49] and Kumar *et al.*[134]

Slightly different from the Z-scheme, the S-scheme can be generated through the inner electric field phenomenon. This

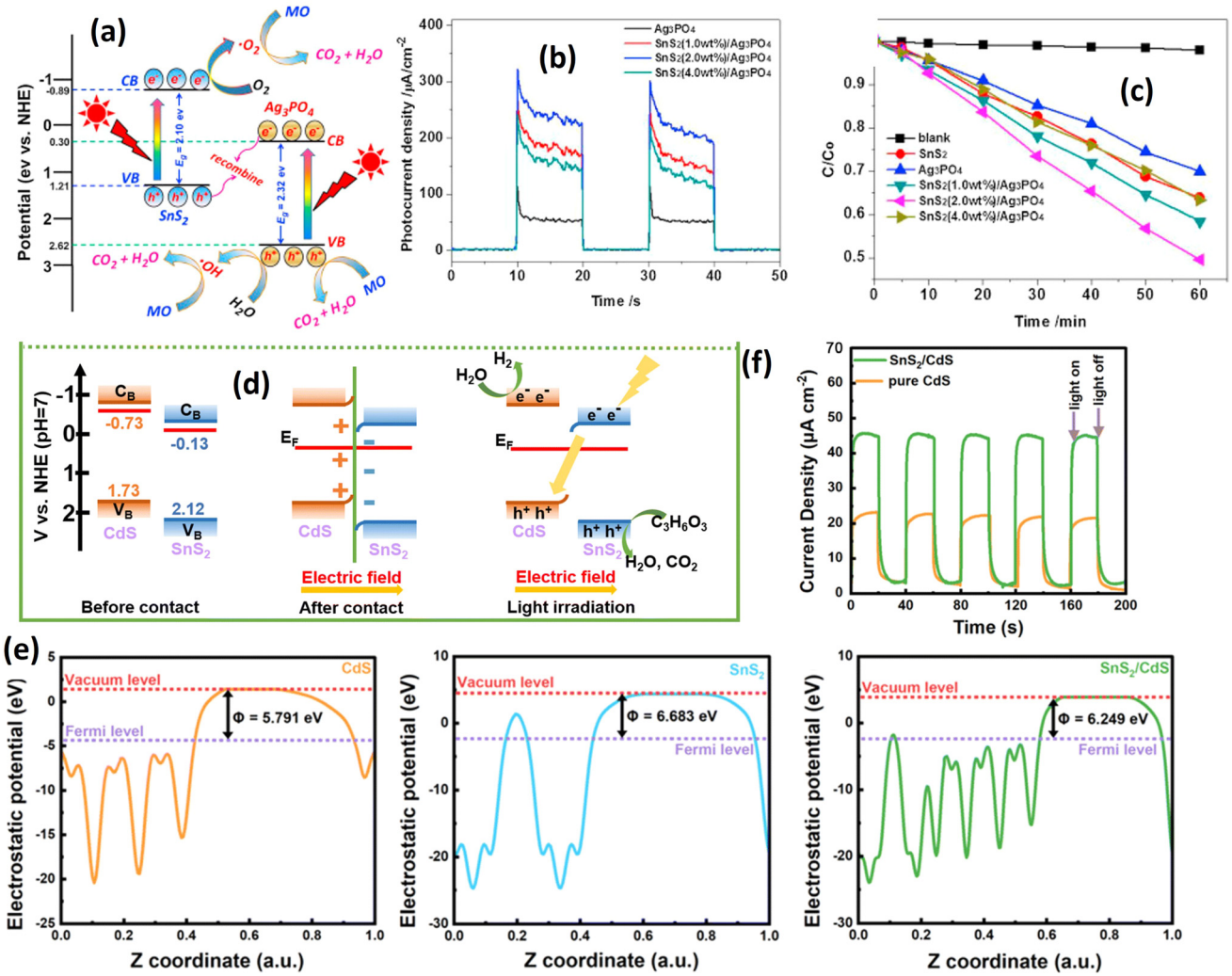

Fig. 14 (a) Schematic diagram of the possible photoinduced electron–hole pair separation process and direct Z-scheme photodegradation mechanism of methyl orange over the SnS_2/Ag_3PO_4 heterojunction photocatalyst under visible light irradiation. (b) Photocurrent response over the as-prepared samples under visible light irradiation. (c) Photocatalytic degradation curves for the photodegradation of MO.[15] (Reproduced from ref. 15 with permission from Elsevier Ltd.) (d) S-scheme illustration of the possible charge transfer processes in the SnS_2/CdS heterostructures; (e) work function analysis of CdS, SnS_2 and SnS_2/CdS. (f) Photocurrent analysis of CdS and SnS_2/CdS.[198] (Reproduced from ref. 198 with permission from the Royal Society of Chemistry.)

electric field emerges when a charge moves between semiconductors, creating a field within each semiconductor due to differing Fermi energies. Fig. 14(d) illustrates an instance of S-scheme formation between SnS_2 and CdS nanoparticles.[198] Before contact, SnS_2 and CdS exhibit different Fermi energy levels; CdS registers at 5.791 eV (Fig. 14(e)), while SnS_2 is at 6.683 eV. Upon interaction, Fermi energy alignment occurs until an equilibrium is established. In this state, the electron density at the SnS_2 interface surpasses that of CdS, generating an inner electric field. Consequently, the valence band of CdS bends, and the conduction band of SnS_2 shows observable curvature. Upon light irradiation, both SnS_2 and CdS generate electron–hole pairs, and the inner electric field facilitates electron transfer from SnS_2 to CdS, enhancing the charge separation efficiency. This improvement is supported by photocurrent analysis (Fig. 14(f)). The photocatalytic activity of the S-scheme SnS_2/CdS photocatalyst for H_2 production, summarized in Table 4, yields 5.18 mmol g^{-1} h^{-1} of hydrogen, 5.95 times higher than that of CdS alone. Similar S-scheme SnS_2-based photocatalysts have been reported for other materials, including BiOBr,[197] SnO_2,[199] $ZnIn_2S_4$.[200]

Table 4 presents various reports on the photocatalytic performance of SnS_2 heterojunction formations. Different strategies yield varying degrees of improvement compared with SnS_2 alone. According to current data, Au/SnS_2 demonstrates a 3.91-fold enhancement over SnS_2. Among the p–n junction formations, $BiFeO_3/SnS_2$ exhibits the most significant improvement, with a degradation rate approximately 7.50 times higher than SnS_2. Similarly, heterojunctions of type I and type II show comparable enhancement, boasting 7.51 times improvements

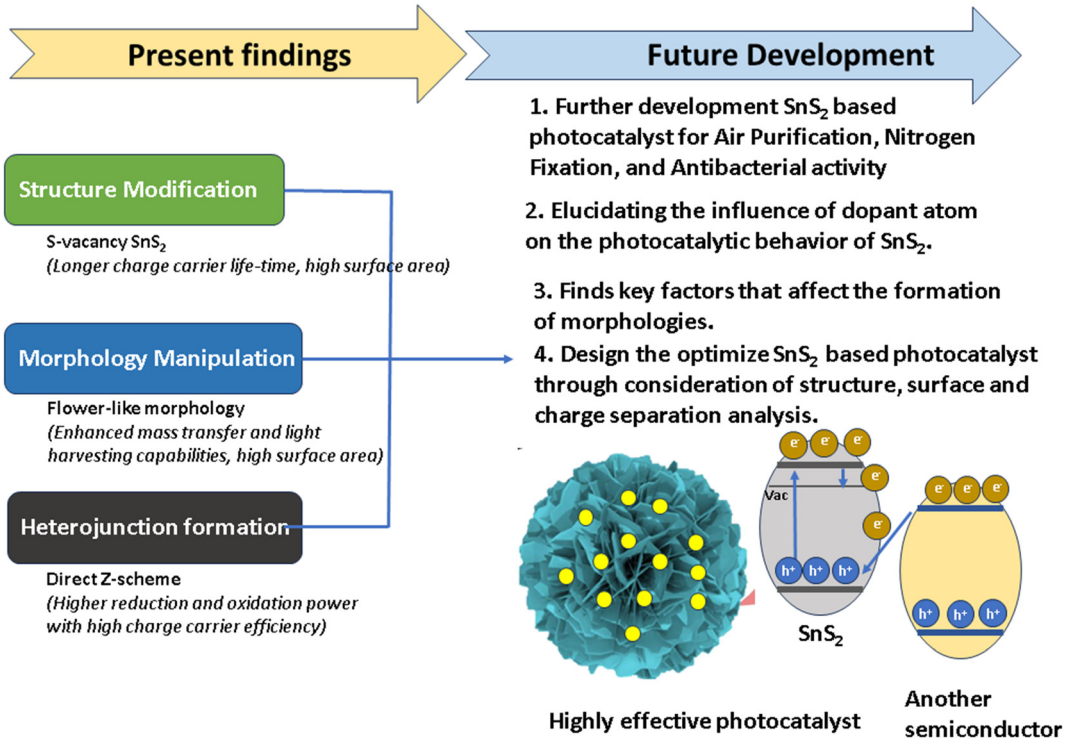

Fig. 15 Current findings and future research direction for SnS_2 photocatalytic research.

over SnS_2. Notably, Z-scheme configurations outperform other heterojunction types, with $BiOBr/SnS_2$ achieving the highest improvement, nearly 75 times higher than SnS_2 alone. This superior enhancement in Z-scheme heterojunctions is attributed to enhanced charge separation efficiency and stronger reduction and oxidation capabilities, resulting in accelerated degradation rates, and increased photochemical reaction yields.

4 Future perspectives

The current strategies for modifying SnS_2 have been thoroughly examined, encompassing structural modification, morphological manipulation, and heterojunction formation. Despite the comprehensive elucidation of each photocatalytic advancement mechanism and synthesis technique in this review, challenges persist, hindering the further advancement of SnS_2 photocatalysts.

In terms of structural modification, it is established that S-vacancies play a pivotal role in enhancing the photocatalytic performance, primarily by improving electron–hole separation efficiency. While the authors attribute this enhancement to electron traps between the valence and conduction bands, empirical evidence remains elusive. Future research endeavors should focus on elucidating the mechanism of the S-vacancy effect on mid-gap formation to substantiate this claim. Additionally, the role of dopants in photocatalytic reactions remains unclear due to their concurrent generation with S-vacancy formation during doping processes. To advance research in this area, techniques minimizing the impact of S-vacancies in doping must be developed to gain a comprehensive understanding of doping phenomena for photocatalytic enhancement.

In morphology engineering, the flower-like morphology has emerged as the most suitable structure for various photocatalytic applications, including wastewater treatment and hydrogen production. Enhanced mass transfer and light harvesting capabilities are key attributes contributing to the photocatalytic performance of flower-like structures. However, challenges in material preparation persist, particularly in hydrothermal synthesis methods, which remain dominant in SnS_2 flower-like morphology production. Although hydrothermal synthesis is known for producing flower-like morphologies, it is important to note that other morphologies can also be generated using the same method and precursor. This variability may hinder further development, as precise control over flower-like morphology parameters such as size, petal-like dimensions, and facet arrangements are essential for further research development of the morphological effect on the photocatalytic performance of SnS_2. Therefore, for future development, it is necessary to find the key factors which control the growth of morphology through hydrothermal reactions encompassing the precursor, solvent, temperature control, and other factors.

While the proliferation of heterojunction formation is widespread, it does not guarantee a comprehensive understanding of photocatalytic mechanisms. Heterostructure formation, con-

sidered one of the most extensively studied systems for SnS_2 photocatalysts, relies on the synergistic effects of its constituent materials. Various types of heterostructure have been reported, each with unique characteristics. Among these, the Z-scheme exhibits significant promise for enhancing photocatalytic performance due to its capacity to augment oxidation and reduction potentials for photocatalytic reactions. However, several considerations must be addressed for the optimal utilization of Z-scheme heterojunction photocatalysts. Beyond the reliance on electronic properties for photocatalytic enhancements, factors such as particle interaction and surface optimization are also pivotal. Particle interaction hinges on the specific facets of each particle, as different facets exhibit distinct electronic and adsorption behaviors. Theoretical investigations, particularly those utilizing density functional theory (DFT) calculations, are essential to fully comprehend these interactions. Additionally, optimizing the surface properties of Z-scheme particles for specific applications, including increasing the surface area and modifying the charge, is imperative for optimizing the adsorption process and enhancing active sites for photocatalytic reactions. To address these issues, for future research directions, it is interesting to employ the comprehensive investigation of photocatalyst design while considering the structural design alongside surface optimization and Z-scheme heterojunction formation.

We have thoroughly discussed the current results and outlined future perspectives for three distinct strategies. Building on this understanding, future research endeavors will focus on integrating these strategies into a unified photocatalyst system. The S-vacancy SnS_2, characterized by a prolonged charge carrier lifetime, can be elaborately engineered into a flower-like morphology with enhanced mass transfer, light harvesting capabilities, and a large surface area. Concurrently, nanoparticles with suitable band gaps, such as CdS and Ag_3VO_4, can be selectively deposited atop the flower-like SnS_2 system for generating a Z-scheme photocatalyst, as illustrated in Fig. 14. The successful amalgamation of these components is anticipated to yield a photocatalyst system of exceptional performance, aligning with industrial standards.

Furthermore, it is imperative to address a critical aspect pertaining to the chemical stability of SnS_2 itself, given its susceptibility to sulfur atom replacement by oxygen upon exposure to air. Factors influencing stability, including the synthesis process and the photocatalyst environment, necessitate meticulous examination. Such analysis assumes paramount importance for practical applications, wherein long-term stability is imperative for industrial viability.

5 Summary

For summarizing this review, Fig. 15 was used for understanding the current findings and future directions. In this review, we have summarized recent strategies for improving the photocatalytic performance of SnS_2, focusing on three fundamental approaches: crystal structure engineering, morphology engineering, and heterojunction formation. SnS_2-based photocatalysts have been utilized in various applications, including CO_2 reduction, H_2 production, nitrogen fixation, antibacterial activity, air purification, and wastewater treatment technologies.

At the current stage, the structural engineering of SnS_2 has been carried out through two methods: vacancy generation and doping processes. These approaches have successfully increased the photocatalytic performance of SnS_2. The fundamental phenomenon observed in S-vacancy generation and doping processes is the ability to decrease the recombination of electrons and holes, thereby facilitating redox reactions. Additionally, altering crystal structures results in a decrease in the crystallite size of SnS_2, which is beneficial for increasing the surface area and the number of active sites for chemical reactions.

Various morphologies of SnS_2, such as flower-like structures, nanoparticles, nanosheets, and quantum dots, exhibit distinct effects on the photocatalytic performance. Flower-like structures, with their high specific surface area and unique morphology, demonstrate superior light harvesting ability and increased active sites compared with nanosheet and nanoparticle morphologies. Although nanosheets have a smaller surface area than flower-like structures, they facilitate the efficient migration of photogenerated electrons and holes to reaction sites, thereby enhancing the photocatalytic efficiency. Conversely, nanoparticle morphology is influenced by the size of the nanoparticles; smaller nanoparticles also contribute to an improved specific surface area, thereby enhancing photocatalytic activity.

Heterojunction formation is by far the most effective strategy for improving photocatalytic reactions, as it enables the generation of synergistic effects between SnS_2 and other materials, significantly enhancing the photocatalytic efficiency. Among various types of heterojunction, Z-scheme photocatalytic reactions are the most promising strategy for improving the photocatalytic performance of SnS_2. This is due to their stronger oxidation and reduction capabilities, coupled with highly efficient charge carrier separation efficiency.

For further development, several aspects are still limited in current literature. Firstly, there is a lack of research on the application of SnS_2 for antibacterial activity, N_2 fixation, and air purification. Therefore, future research should focus more on investigating these types of photocatalytic application. Secondly, there is uncertainty regarding the effect of dopants on vacancy generation. Since the doping process directly leads to vacancy formation, the individual impact of each dopant is not well understood. To address this issue, both synthesis processes and theoretical approaches should be conducted simultaneously to comprehensively understand the doping effect on improving charge carrier separation in SnS_2. Moreover, the growth of morphology is not well understood. Therefore, for future development, it is necessary to find the key factor which controls the growth of morphology through hydrothermal reactions encompassing precursor, solvent, temperature control, and other factors.

However, one of the most crucial areas of research is the design of the ideal photocatalyst based on the aforementioned findings. Developing a Z-scheme SnS_2-based photocatalyst with a high specific surface area and efficient charge carrier separation is essential. One promising technique is to combine SnS_2 flower-like structures with very small nanoparticles, allowing the particles to attach to the flower-like structures, thereby improving the light harvesting process and charge carrier separation efficiency. Lastly, the stability of SnS_2 is a critical consideration. Since SnS_2 is prone to oxidation, stability studies must be conducted to meet industrial standards.

Conflicts of interest

There are no conflicts to declare.

Acknowledgements

This study was supported by the research grant of The University of Suwon in 2023.

References

1 R. Yang, Y. Fan, Y. Zhang, L. Mei, R. Zhu, J. Qin, J. Hu, Z. Chen, Y. Hau Ng, D. Voiry, S. Li, Q. Lu, Q. Wang, J. C. Yu and Z. Zeng, *Angew. Chem., Int. Ed.*, 2023, **62**, 1–29.
2 W. Peng, Y. Li, F. Zhang, G. Zhang and X. Fan, *Ind. Eng. Chem. Res.*, 2017, **56**, 4611–4626.
3 V. Dhiman and N. Kondal, *Phys. B*, 2022, **628**, 413569.
4 W. Yu, X. Chen, W. Mei, C. Chen and Y. Tsang, *Appl. Surf. Sci.*, 2017, **400**, 129–138.
5 R. A. Geioushy, I. M. Hegazy, S. M. El-Sheikh and O. A. Fouad, *J. Environ. Chem. Eng.*, 2022, **10**, 107337.
6 Y. J. Huang, L. M. Lyu, C. Y. Lin, G. C. Lee, K. Y. Hsiao and M. Y. Lu, *ACS Omega*, 2022, **7**, 2217–2223.
7 B. Chen, Y. Meng, J. Sha, C. Zhong, W. Hu and N. Zhao, *Nanoscale*, 2018, **10**, 34–68.
8 Y. Lin, P. Ren and C. Wei, *CrystEngComm*, 2019, **21**, 3439–3450.
9 E. C. Cho, C. W. Chang-Jian, J. H. Zheng, J. H. Huang, K. C. Lee, B. C. Ho and Y. S. Hsiao, *J. Taiwan Inst. Chem. Eng.*, 2018, **91**, 489–498.
10 W. Ho, J. C. Yu, J. Lin, J. Yu and P. Li, *Langmuir*, 2004, **20**, 5865–5869.
11 X. Zhang, K. Zhu, C. Xie and P. Yang, *Carbon*, 2024, **220**, 118884.
12 Y. Chen, H. Sun and W. Peng, *Nanomaterials*, 2017, **7**, 1–11.
13 R. Tong, K. W. Ng, X. Wang, S. Wang, X. Wang and H. Pan, *J. Mater. Chem. A*, 2020, **8**, 23202–23230.
14 L. Han, Y. L. Zhong, K. Lei, D. Mao, Y. Z. Dong, G. Hong, Y. T. Zhou and D. Fang, *J. Phys. Chem. C*, 2019, **123**, 2398–2409.
15 J. Luo, X. Zhou, L. Ma, L. Xu, X. Xu, Z. Du and J. Zhang, *Mater. Res. Bull.*, 2016, **81**, 16–26.
16 X. Hu, G. Song, W. Li, Y. Peng, L. Jiang, Y. Xue, Q. Liu, Z. Chen and J. Hu, *Mater. Res. Bull.*, 2013, **48**, 2325–2332.
17 Y. Shan, Y. Li and H. Pang, *Adv. Funct. Mater.*, 2020, **30**, 200198.
18 H. Li, Q. Su, J. Kang, H. Feng, P. Huang, M. Feng, M. Huang and G. Du, *Mater. Res. Bull.*, 2018, **108**, 106–112.
19 W. J. Yan, D. Y. Chen, H. R. Fuh, Y. L. Li, D. Zhang, H. Liu, G. Wu, L. Zhang, X. Ren, J. Cho, M. Choi, B. S. Chun, C. Coileáin, H. J. Xu, Z. Wang, Z. Jiang, C. R. Chang and H. C. Wu, *RSC Adv.*, 2019, **9**, 626–635.
20 J. Sun, W. Xiong, J. Zhang, Y. Zhang and B. Xie, *Mater. Lett.*, 2021, **308**, 131214.
21 C. S. Diko, M. Abitonze, Y. Liu, Y. Zhu and Y. Yang, *Nanomaterials*, 2022, **12**, 4497.
22 D. Ma, W. Zhang, Q. Tang, R. Zhang, W. Yu and Y. Qian, *J. Nanosci. Nanotechnol.*, 2005, **5**, 806–809.
23 H. Zhu, X. Ji and D. Yang, *J. Mater. Sci.*, 2006, **41**, 3489–3492.
24 R. K. Mishra, G. W. Baek, K. Kim, H. I. Kwon and S. H. Jin, *Appl. Surf. Sci.*, 2017, **425**, 923–931.
25 B. Hai, K. Tang, C. Wang, C. An, Q. Yang, G. Shen and Y. Qian, *J. Cryst. Growth*, 2001, **225**, 92–95.
26 A. Sánchez-Juárez, A. Tiburcio-Silver and A. Ortiz, *Thin Solid Films*, 2005, **480–481**, 452–456.
27 G. Su, V. G. Hadjiev, P. E. Loya, J. Zhang, S. Lei, S. Maharjan, P. Dong, P. M. Ajayan, J. Lou and H. Peng, *Nano Lett.*, 2015, **15**, 506–513.
28 J. Johny, S. S. Guzman, B. Krishnan, J. A. A. Martinez, D. Avellaneda Avellaneda and S. Shaji, *Appl. Surf. Sci.*, 2019, **470**, 276–288.
29 J. Johny, S. Sepulveda-Guzman, B. Krishnan, D. Avellaneda and S. Shaji, *Appl. Surf. Sci.*, 2018, **435**, 1285–1295.
30 W. Wang, T. Zhang, A. Seliverstov, H. Zhang, Y. Wang, F. Wang, X. Peng, Q. Lu, C. Qin, X. Pan, Y. J. Zeng, C. Van Haesendonck and Z. Ye, *Adv. Electron. Mater.*, 2019, **6**, 1901020.
31 S. R. Damkale, S. S. Arbuj, G. G. Umarji, R. P. Panmand, S. K. Khore, R. S. Sonawane, S. B. Rane and B. B. Kale, *Sustainable Energy Fuels*, 2019, **3**, 3406–3414.
32 N. Jawale, S. Arbuj, G. Umarji, M. Shinde, B. Kale and S. Rane, *RSC Adv.*, 2023, **13**, 2418–2426.
33 A. C. Ok and C. Sarıoğlu, *Int. J. Hydrogen Energy*, 2024, **52**, 561–568.
34 B. Balan, M. M. Xavier and S. Mathew, *ACS Omega*, 2023, **8**, 25649–25673.
35 T. Qiang, L. Chen, Y. Xia and X. Qin, *J. Cleaner Prod.*, 2021, **291**, 125213.
36 X. Bai, Y. Du, W. Xue, X. Hu, J. Fan, J. Li and E. Liu, *Nanoscale Adv.*, 2020, **2**, 4220–4228.

37 M. Faisal, J. Ahmed, J. S. Algethami, A. S. Alkorbi and F. A. Harraz, *J. Saudi Chem. Soc.*, 2024, **28**, 101806.
38 X. Zou, B. Sun, L. Wang, H. Bai, X. Meng, C. Li and Z. Li, *Chem. Eng. J.*, 2024, **482**, 148818.
39 P. Huang, F. Chen, Y. Tang, W. Sun, Y. Song and Y. Sun, *Mater. Sci. Semicond. Process.*, 2024, **173**, 108182.
40 A. Fakhri, S. Behrouz and M. Pourmand, *J. Photochem. Photobiol., B*, 2015, **149**, 45–50.
41 A. Fakhri and S. Behrouz, *Sol. Energy*, 2015, **117**, 187–191.
42 V. Gadore, S. R. Mishra and M. Ahmaruzzaman, *J. Hazard. Mater.*, 2023, **461**, 132458.
43 A. N. Ech-Chergui, F. Bennabi, M. Isik, Y. Khane, F. J. G. García, A. S. Kadari, M. Guezzoul, A. Rahman, M. M. Khan, A. Mehdi, K. Driss-Khodja and B. Amrani, *Colloids Surf., A*, 2024, **686**, 133362.
44 F. Chang, Z. Wei, Z. Zhao, Y. Qi and D. Liu, *J. Ind. Eng. Chem.*, 2023, **117**, 265–272.
45 J. Yu, C. Y. Xu, F. X. Ma, S. P. Hu, Y. W. Zhang and L. Zhen, *ACS Appl. Mater. Interfaces*, 2014, **6**, 22370–22377.
46 H. P. Nogueira, S. H. Toma, A. T. Silveira, A. A. C. Carvalho, A. M. Fioroto and K. Araki, *Microchem. J.*, 2019, **149**, 104025.
47 J. R. Tu, X. F. Shi, H. W. Lu, N. X. Yang and Y. J. Yuan, *Mater. Lett.*, 2016, **185**, 303–306.
48 T. Qiang and Y. Xia, *J. Alloys Compd.*, 2020, **845**, 156155.
49 L. Li, Y. Du, H. Sun, H. Zhang and Z. Zhong, *ChemCatChem*, 2022, **15**, 1436.
50 J. Zai, X. Wei, M. Sun, H. Tian, X. Liu, R. Qi and X. Qian, *J. Photochem. Photobiol., A*, 2021, **415**, 113320.
51 B. Xia, F. Deng, S. Zhang, L. Hua, X. Luo and M. Ao, *J. Hazard. Mater.*, 2020, **392**, 122345.
52 S. Singla, S. Basu and P. Devi, *J. Ind. Eng. Chem.*, 2023, **118**, 119–131.
53 M. Kovacic, J. Papac, H. Kusic, P. Karamanis and A. Loncaric Bozic, *Chem. Eng. J.*, 2020, **381**, 1222826.
54 N. Afzali, M. Torka Beydokhti, A. A. Khodadadi and Y. Mortazavi, *J. Environ. Chem. Eng.*, 2022, **10**, 107793.
55 G. Lu, X. Xie, X. Wang, G. Shi, Q. Zeng, D. Segets and J. Sun, *J. Photochem. Photobiol., A*, 2018, **364**, 725–731.
56 A. K. Ganguli, G. B. Kunde, W. Raza, S. Kumar and P. Yadav, *Molecules*, 2022, **27**(22), 7778.
57 Y. Liu, D. A. Cullen and T. Lian, *J. Am. Chem. Soc.*, 2021, **143**, 20264–20273.
58 W. Gao, J. Lu, S. Zhang, X. Zhang, Z. Wang, W. Qin, J. Wang, W. Zhou, H. Liu and Y. Sang, *Adv. Sci.*, 2019, **6**, 1244.
59 B. Ohtani, *Catalysts*, 2013, **3**, 942–953.
60 F. Amano, K. Nogami, M. Tanaka and B. Ohtani, *Langmuir*, 2010, **26**, 7174–7180.
61 H. Cheng, J. Wang, Y. Zhao and X. Han, *RSC Adv.*, 2014, **4**, 47031–47038.
62 N. Roy, Y. Park, Y. Sohn, K. T. Leung and D. Pradhan, *ACS Appl. Mater. Interfaces*, 2014, **6**, 16498–16507.
63 Z. Zheng, Z. Wang, L. Xie, Z. Fang, W. Feng, M. Huang and P. Liu, *Appl. Surf. Sci.*, 2015, **353**, 714–722.
64 X. Zhang, C. Bo, S. Cao, Z. Cheng, Z. Xiao, X. Liu, T. Tan and L. Piao, *J. Mater. Chem. A*, 2022, **10**, 24381–24387.
65 R. A. Carcel, L. Andronic and A. Duta, *Mater. Charact.*, 2012, **70**, 68–73.
66 L. Jiang, Z. Y. Jiang, Y. M. Lin and J. M. Zheng, *Phys. Status Solidi RRL*, 2021, **15**, 340.
67 I. Shown, S. Samireddi, Y. C. Chang, R. Putikam, P. H. Chang, A. Sabbah, F. Y. Fu, W. F. Chen, C. I. Wu, T. Y. Yu, P. W. Chung, M. C. Lin, L. C. Chen and K. H. Chen, *Nat. Commun.*, 2018, **9**(1), 169.
68 X. Shuai, Y. Wang, J. Zhang, R. Zhao, T. Guo, J. Du and J. Li, *ChemistrySelect*, 2022, **7**(33), 1068.
69 J. H. Liu, G. F. Huang, W. Q. Huang, H. Miao and B. X. Zhou, *Mater. Lett.*, 2015, **161**, 480–483.
70 Y. Zhao, D. Sun, K. Hu, W. Zhao and F. Huang, *Inorg. Chem. Commun.*, 2020, **114**, 107849.
71 S. Mondal, S. Das and U. K. Gautam, *J. Colloid Interface Sci.*, 2021, **603**, 110–119.
72 S. Paul, D. Barman, C. Chowdhury, P. K. Giri and S. K. De, *CrystEngComm*, 2021, **23**, 2276–2288.
73 F. Zhang, L. Shen, J. Li, Y. Zhang, G. Wang and A. Zhu, *Powder Technol.*, 2021, **383**, 371–380.
74 Y. Liu, D. Pan, M. Xiong, Y. Tao, X. Chen, D. Zhang, Y. Huang and G. Li, *Chin. J. Catal.*, 2020, **41**, 1554–1563.
75 A. Bumajdad and M. Madkour, *Phys. Chem. Chem. Phys.*, 2014, **16**, 7146–7158.
76 M. Lin, H. Chen, Z. Zhang and X. Wang, *Phys. Chem. Chem. Phys.*, 2023, **25**, 4388–4407.
77 K. Sharma, S. Patial, P. Singh, A. A. P. Khan, V. Saini, A. K. Nadda, C. M. Hussain, V. H. Nguyen, C. C. Nguyen, T. B. Hac Nguyen, S. Y. Kim, Q. Van Le and P. Raizada, *Sol. Energy*, 2022, **231**, 546–565.
78 X. Guo, F. Zhang, Y. Zhang and J. Hu, *J. Mater. Chem. A*, 2023, **11**, 7331–7343.
79 L. A. Burton, T. J. Whittles, D. Hesp, W. M. Linhart, J. M. Skelton, B. Hou, R. F. Webster, G. O'Dowd, C. Reece, D. Cherns, D. J. Fermin, T. D. Veal, V. R. Dhanak and A. Walsh, *J. Mater. Chem. A*, 2016, **4**, 1312–1318.
80 S. Deng, Y. Chen, Q. Li, J. Sun, Z. Lei, P. Hu, Z. H. Liu, X. He and R. Ma, *Nanoscale*, 2022, **14**, 14097–14105.
81 P. Shinde and C. S. Rout, *Mater. Chem. Front.*, 2021, **5**, 516–556.
82 W. Zhao, Z. Wei, L. Ma, J. Liang and X. Zhang, *Materials*, 2019, **12**(4), 582.
83 H. Y. He, J. Lu, L. Y. Cao and M. Li, *Res. Chem. Intermed.*, 2012, **38**, 537–547.
84 L. Dashairya, M. Sharma, S. Basu and P. Saha, *J. Alloys Compd.*, 2019, **774**, 625–636.
85 R. R. Srivastava, P. Kumar Vishwakarma, U. Yadav, S. Rai, S. Umrao, R. Giri, P. S. Saxena and A. Srivastava, *Front. Nanotechnol.*, 2021, **3**, 711368.
86 Z. Li, R. Fan, Z. Hu, W. Li, H. Zhou, S. Kang, Y. Zhang, H. Zhang and G. Wang, *J. Hazard. Mater.*, 2020, **394**, 122525.
87 V. Govindan, H. Imran, V. Dharuman and K. Sankaranarayanan, *J. Mater. Sci.: Mater. Electron.*, 2018, **29**, 17670–17680.
88 Z. Liu, C. Liu, S. Mao and X. Huang, *ACS Appl. Mater. Interfaces*, 2023, **15**, 7529–7537.

89 Y. Kawabe, Y. Ito, Y. Hori, S. Kukunuri, F. Shiokawa, T. Nishiuchi, S. Jeong, K. Katagiri, Z. Xi, Z. Li, Y. Shigeta and Y. Takahashi, *ACS Nano*, 2023, **17**, 11318–11326.
90 H. Wang, Z. Liu, L. Wang, Q. Shou, M. Gao, H. Wang, A. Nazir and P. Huo, *J. Mater. Sci.: Mater. Electron.*, 2023, **34**, 350.
91 C. Jin, W. Feng and X. Zhao, *IOP Conference Series: Earth and Environmental Science*, IOP Publishing Ltd, 2021, vol. 766.
92 Y. Nie, J. Liu, N. Li, Y. Wang, Q. Cheng, S. He, Q. Guo, R. Zhao and F. Pan, *Fuel Process. Technol.*, 2023, **250**, 107871.
93 L. Xiang, S. Liu, L. Zhao, S. Yuan, X. Li and N. Li, *J. Alloys Compd.*, 2023, **945**, 169201.
94 M. Lan, X. Dong, N. Zheng, X. Zhang, Y. Wang and X. Zhang, *J. Mater. Sci. Technol.*, 2023, **167**, 237–247.
95 S. R. Kadam, S. Ghosh, R. Bar-Ziv and M. Bar-Sadan, *Chem. – Eur. J.*, 2020, **26**, 6679–6685.
96 J. W. Shi, Y. Zou, D. Ma, Z. Fan, L. Cheng, D. Sun, Z. Wang, C. Niu and L. Wang, *Nanoscale*, 2018, **10**, 9292–9303.
97 T. Di, T. Cao, H. Liu, S. Wang and J. Zhang, *Phys. Chem. Chem. Phys.*, 2023, **25**, 5196–5202.
98 A. R. Woldu, P. Talebi, A. G. Yohannes, J. Xu, X. D. Wu, S. Siahrostami, L. Hu and X. C. Huang, *Angew. Chem., Int. Ed.*, 2023, **62**, e2023016.
99 T. Billo, I. Shown, A. Anbalagan, T. A. Effendi, A. Sabbah, F. Y. Fu, C. M. Chu, W. Y. Woon, R. S. Chen, C. H. Lee, K. H. Chen and L. C. Chen, *Nano Energy*, 2020, **72**, 104717.
100 X. Jiao, X. Li, X. Jin, Y. Sun, J. Xu, L. Liang, H. Ju, J. Zhu, Y. Pan, W. Yan, Y. Lin and Y. Xie, *J. Am. Chem. Soc.*, 2017, **139**, 18044–18051.
101 G. Li, W. Liu, J. Wang, B. Li, S. Yang, W. Wang, W. Sun and Y. Sun, *Chem. Phys. Lett.*, 2022, **807**, 140063.
102 G. Ma, Z. Pan, Y. Liu, Y. Lu and Y. Tao, *Materials*, 2023, **16**, 4436.
103 G. Kumar, J. Kumar, M. Bag and R. Kumar Dutta, *Sep. Purif. Technol.*, 2022, **292**, 121040.
104 G. Kumar and R. K. Dutta, *Environ. Sci. Pollut. Res.*, 2022, **29**, 57758–57772.
105 Y. C. Zhang, Z. N. Du, K. W. Li and M. Zhang, *Sep. Purif. Technol.*, 2011, **81**, 101–107.
106 L. Li, Z. Chai, W. Jin, H. Sun, J. He, G. Wu and W. Xia, *J. Alloys Compd.*, 2023, **932**, 167658.
107 X. Zhang and P. Yang, *Carbon*, 2024, **216**, 118584.
108 Y. Sun, G. Li, J. Xu and Z. Sun, *Mater. Lett.*, 2016, **174**, 238–241.
109 G. Li, Y. Sun, S. Sun, W. Chen, J. Zheng, F. Chen, Z. Sun and W. Sun, *Adv. Powder Technol.*, 2020, **31**, 2505–2512.
110 F. Wang, S. Zhang, W. Jing, H. Qiu, Y. Liu and L. Guo, *J. Mater. Sci. Technol.*, 2024, **189**, 146–154.
111 T. Song, X. Zhang, C. Xie and P. Yang, *Carbon*, 2023, **210**, 118052.
112 K. Perović, M. Kovačić, M. Kraljić Roković, H. Kušić, B. Genorio, U. Lavrenčić Štangar and A. Lončarić Božić, *Mater. Res. Bull.*, 2023, **167**, 112418.
113 J. Wang, J. Xuan, X. Wei, Y. Zhang, J. Fan, L. Ni, Y. Yang, J. Liu, Y. Tian and L. Duan, *Int. J. Hydrogen Energy*, 2024, **54**, 979–989.
114 Y. Li, Z. Liu, S. Wu, M. Zhu and Y. Zhang, *Chem. Phys. Lett.*, 2022, **812**, 140248.
115 M. Awais, S. Aslam, M. N. Ashiq, M. Mirza and M. Safdar, *New J. Chem.*, 2024, **48**, 3247–3257.
116 P. A. K. Reddy, H. Han, K. C. Kim and S. Bae, *ACS Sustainable Chem. Eng.*, 2024, **12**, 4979–4992.
117 N. Ma, C. Lu, Y. Liu, T. Han, W. Dong, D. Wu and X. Xu, *Small*, 2024, **20**, 2304839.
118 A. Fakhri, S. Behrouz and M. Pourmand, *J. Photochem. Photobiol., B*, 2015, **149**, 45–50.
119 X. Zhang, P. Yang, H. S. Chen and S. P. Jiang, *Chem. Eng. J.*, 2023, **479**, 147609.
120 D. Wang, P. Zhao, J. Yang, G. Xu, H. Yang, Z. Shi, Q. Hu, B. Dong and Z. Guo, *Colloids Surf., A*, 2020, **603**, 125147.
121 S. Thirumalairajan, K. Girija, V. R. Mastelaro and N. Ponpandian, *New J. Chem.*, 2014, **38**, 5480–5490.
122 K. Tamilarasu, R. Ranjith, P. Maadeswaran, R. Ramesh, R. Thammasak, G. Periyasami, P. Karthikeyan and C. Umarani, *J. Mater. Sci.: Mater. Electron.*, 2024, **35**, 607.
123 Y. Ben Smida, O. Oyewo, S. Ramaila, L. Mavuru, R. Marzouki, D. C. Onwudiwe and A. H. Hamzaoui, *J. Inorg. Organomet. Polym. Mater.*, 2022, **32**, 4679–4693.
124 Y. Cheng, J. He and P. Yang, *Colloids Surf., A*, 2023, **680**, 132678.
125 K. M. Alnahdi, *Inorg. Chem. Commun.*, 2023, **160**, 111870.
126 X. Zheng, M. Xu, C. Cai, Y. Yuan, F. Lin, W. Chen and F. Yang, *J. Alloys Compd.*, 2024, **980**, 173630.
127 V. Gadore, S. R. Mishra and M. Ahmaruzzaman, *J. Hazard. Mater.*, 2023, **444**, 130301.
128 S. Park, R. Selvaraj, M. A. Meetani and Y. Kim, *J. Ind. Eng. Chem.*, 2017, **45**, 206–214.
129 X. Wu, H. Hu, L. Cheng, Y. Zhang, Q. Jiang, P. Wang, L. Xu, P. Lin and C. Cui, *J. Mater. Sci.: Mater. Electron.*, 2024, **35**, 545.
130 P. Cao, Y. Zhang, D. Gao, H. Chen, M. Zhou, Y. He, P. Song and R. Wang, *J. Alloys Compd.*, 2022, **904**, 164061.
131 T. T. Salunkhe, V. Kumar, A. N. Kadam, M. Mali and M. Misra, *Ceram. Int.*, 2024, **50**, 1826–1835.
132 G. Kumar, *J. Inorg. Organomet. Polym. Mater.*, 2023, **33**, 2710–2720.
133 M. Rajamani, A. Rajan and B. Neppolian, *J. Environ. Chem. Eng.*, 2022, **11**, 109129.
134 G. Kumar and R. K. Dutta, *J. Phys. Chem. Solids*, 2022, **164**, 110639.
135 F. You, X. Hou, P. Wei and J. Qi, *Inorg. Chem.*, 2021, **60**(24), 18598–18602.
136 F. You, Y. Zhou, D. Li, H. Zhang, D. Gao, X. Ma, R. Hao and J. Liu, *J. Colloid Interface Sci.*, 2023, **629**, 871–877.
137 T. Di, B. Zhu, B. Cheng, J. Yu and J. Xu, *J. Catal.*, 2017, **352**, 532–541.
138 N. Jawale, S. Arbuj, G. Umarji, M. Shinde, B. Kale and S. Rane, *RSC Adv.*, 2023, **13**, 2418–2426.

139 G. Li, Y. Sun, X. Hong, W. Lu, W. Chen, Y. Deng, Z. Sun and W. Sun, *J. Mater. Sci.*, 2021, **56**, 10847–10858.
140 S. Zhu, G. Wu, Z. Liu, S. Zhao, D. Cao, C. Li and G. Liu, *Ceram. Int.*, 2023, **49**, 5893–5904.
141 H. Zhao, B. Zhao, H. Liu and X. Li, *Dalton Trans.*, 2023, **53**, 591–600.
142 F. Ganaie, Z. Haq, A. Bashir, A. Qureashi, I. Nazir, K. Fatima, A. H. Pandith and M. A. Bhat, *New J. Chem.*, 2024, **48**, 7111–7124.
143 S. Q. Guo, B. Yang, Z. Hu, M. Zhen, B. Gu and B. Shen, *Nano Res.*, 2023, **16**, 2102–2110.
144 S. Liu, *Mater. Lett.*, 2023, **330**, 133256.
145 X. He, T. He, R. Xia, Y. Qi, Y. Zhou, B. Song, F. Liao, Z. Kang and L. Jiang, *Sep. Purif. Technol.*, 2023, **324**, 124515.
146 Z. Wan, Q. Mao, J. Xiang, D. Ma and H. Tang, *J. Mater. Sci. Technol.*, 2023, **161**, 233–244.
147 S. Kar, T. Pal and S. Ghosh, *ChemistrySelect*, 2023, **8**, e202300878.
148 S. Bai, N. Zhang, C. Gao and Y. Xiong, *Nano Energy*, 2018, **53**, 296–336.
149 J. Liu, Z. Wei and W. Shangguan, *ChemCatChem*, 2019, **11**, 6177–6189.
150 H. Zhang, L. Mao, J. Wang, Y. Nie, Z. Geng, D. Zhong, X. Tan, J. Ye and T. Yu, *Small*, 2023, **20**, 5727.
151 M. Chen, S. Wan, L. Zhong, D. Liu, H. Yang, C. Li, Z. Huang, C. Liu, J. Chen, H. Pan, D. S. Li, S. Li, Q. Yan and B. Liu, *Angew. Chem., Int. Ed.*, 2021, **60**, 26233–26237.
152 G. Kiruthigaa, C. Manoharan, M. Bououdina, S. Ramalingam and C. Raju, *Solid State Sci.*, 2015, **44**, 32–38.
153 Y. Liu, Y. Zhou, X. Zhou, X. Jin, B. Li, J. Liu and G. Chen, *Chem. Eng. J.*, 2021, **407**, 127180.
154 A. Sharma, A. Makhija, S. Dahiya, A. Ohlan, R. Punia and A. S. Maan, *Mater. Res. Bull.*, 2023, **168**, 112464.
155 M. Setayeshmehr, M. Haghighi and K. Mirabbaszadeh, *Electrochim. Acta*, 2021, **376**, 137987.
156 P. Bharathi, S. Harish, M. Shimomura, M. Krishna Mohan, J. Archana and M. Navaneethan, *Mater. Lett.*, 2023, **335**, 133691.
157 P. Sengodu, C. H. Li, C. F. Wei, R. Bendi and C. C. Chen, *ChemistrySelect*, 2016, **1**, 3328–3334.
158 C. Mondal, M. Ganguly, J. Pal, A. Roy, J. Jana and T. Pal, *Langmuir*, 2014, **30**, 4157–4164.
159 X. Zhang, A. Chen, L. Chen and Z. Zhou, *Adv. Energy Mater.*, 2022, **12**, 2003841.
160 Y. Hu, X. Chen, X. Ren, Z. Huang, X. Qi and J. Zhong, *J. Mater. Sci.: Mater. Electron.*, 2018, **29**, 19614–19619.
161 B. Luo, G. Liu and L. Wang, *Nanoscale*, 2016, **8**, 6904–6920.
162 J. Zhang, G. Huang, J. Zeng, X. Jiang, Y. Shi, S. Lin, X. Chen, H. Wang, Z. Kong, J. Xi and Z. Ji, *J. Alloys Compd.*, 2019, **775**, 726–735.
163 Y. Liu, X. Mi, J. Wang, M. Li, D. Fan, H. Lu and X. Chen, *Inorg. Chem. Front.*, 2019, **6**, 948–954.
164 Y. C. Zhang, J. Li, M. Zhang and D. D. Dionysiou, *Environ. Sci. Technol.*, 2011, **45**, 9324–9331.
165 J. Gajendiran and V. Rajendran, *Adv. Nat. Sci.: Nanosci. Nanotechnol.*, 2021, **2**(1), 15001.
166 S. H. Chaki, M. P. Deshpande, D. P. Trivedi, J. P. Tailor, M. D. Chaudhary and K. Mahato, *Appl. Nanosci.*, 2013, **3**, 189–195.
167 X. L. Gou, J. Chen and P. W. Shen, *Mater. Chem. Phys.*, 2005, **93**, 557–566.
168 Y. Ren, H. An, W. Zhang, S. Wei, C. Xing and Z. Peng, *Nanophotonics*, 2022, **11**, 4781–4792.
169 H. Zhao, X. Li, Y. Chen, Z. Zhao, M. Zhang, H. Su, H. Liang, W. Zhang, K. Tao and L. Li, *J. Lumin.*, 2023, **235**, 118068.
170 Y. Huang, W. Jiao, Z. Chu, X. Nie, R. Wang and X. He, *ACS Appl. Mater. Interfaces*, 2020, **12**, 25178–25188.
171 Y. J. Yuan, D. Q. Chen, X. F. Shi, J. R. Tu, B. Hu, L. X. Yang, Z. T. Yu and Z. G. Zou, *Chem. Eng. J.*, 2017, **313**, 1438–1446.
172 T. Ali, X. Wang, K. Tang, Q. Li, S. Sajjad, S. Khan, S. A. Farooqi and C. Yan, *Electrochim. Acta*, 2019, **300**, 45–52.
173 B. Wang, M. Chen, J. Lv, G. Xu, X. Shu and Y. C. Wu, *Dalton Trans.*, 2021, **50**, 13329–13336.
174 D. Ursu, M. Vajda and M. Miclau, *Micro Nano Lett.*, 2019, **14**, 872–876.
175 Y. Liang, N. Guo, L. Li, R. Li, G. Ji and S. Gan, *Appl. Surf. Sci.*, 2015, **332**, 32–39.
176 J. M. Mali, S. S. Arbuj, J. D. Ambekar, S. B. Rane, U. P. Mulik and D. P. Amalnerkar, *Sci. Adv. Mater.*, 2013, **5**, 1994–1998.
177 Z. Liu, K. Xu, H. Yu and Z. Sun, *Int. J. Energy Res.*, 2021, **45**, 6850–6862.
178 L. L. Zulfa, R. Ediati, A. R. P. Hidayat, R. Subagyo, N. Faaizatunnisa, Y. Kusumawati, D. Hartanto, N. Widiastuti, W. P. Utomo and M. Santoso, *RSC Adv.*, 2023, **13**, 3818–3834.
179 Y. Zhong, C. Peng, Z. He, D. Chen, H. Jia, J. Zhang, H. Ding and X. Wu, *Catal. Sci. Technol.*, 2021, **11**, 27–42.
180 G. Li and K. A. Gray, *Chem. Phys.*, 2007, **339**, 173–187.
181 A. Mohanty and K. Kamali, *ACS Appl. Nano Mater.*, 2024, **7**, 3326–3338.
182 N. R. Barveen, J. L. Xu and Y. W. Cheng, *J. Environ. Chem. Eng.*, 2024, **12**, 112200.
183 J. Feng, Y. Sun, J. Mu, L. Chen, T. Han, H. Miao, E. Liu, J. Fan and X. Hu, *Mater. Lett.*, 2019, **236**, 534–537.
184 S. Mondal, L. Sahoo, C. P. Vinod and U. K. Gautam, *Appl. Catal., B*, 2021, **2**, 119927.
185 S. I. Naya, K. Kimura and H. Tada, *ACS Catal.*, 2013, **3**, 10–13.
186 R. Fu, L. Li, X. Li, B. Li, C. Shao, Z. Liu and A. Shen, *Mater. Chem. Phys.*, 2021, **267**, 124702.
187 T. Wang, H. Meng, X. Yu, Y. Liu, H. Chen, Y. Zhu, J. Tang, Y. Tong and Y. Zhang, *RSC Adv.*, 2015, **5**, 15469–15478.
188 M. Bagherzadeh and R. Kaveh, *J. Photochem. Photobiol., A*, 2018, **359**, 11–22.
189 H. Derikvandi and A. Nezamzadeh-Ejhieh, *J. Colloid Interface Sci.*, 2017, **490**, 628–641.

190 L. Sun, Z. Zhao, S. Li, Y. Su, L. Huang, N. Shao, F. Liu, Y. Bu, H. Zhang and Z. Zhang, *ACS Appl. Nano Mater.*, 2019, **2**, 2144–2151.
191 Q. Liu, S. Liu, A. Wu, H. Huang and L. Zhou, *J. Alloys Compd.*, 2020, **834**, 155174.
192 L. Zhang, X. Dong, Y. Wang, N. Zheng, H. Ma and X. Zhang, *Appl. Surf. Sci.*, 2022, **579**, 152088.
193 L. Wang, S. K. Karuturi and L. Zan, *Appl. Surf. Sci.*, 2023, **537**, 148063.
194 Y. Liu, C. Lv, J. Sun, X. Zhou, Y. Zhou and G. Chen, *Adv. Mater. Interfaces*, 2022, **9**, 2200153.
195 Sunaina, K. K. Yadav, Ankush, S. K. Guchhait, K. Sood, S. K. Mehta, A. K. Ganguli and M. Jha, *Sep. Purif. Technol.*, 2020, **242**, 116835.
196 J. Pan, Z. Guan, J. Yang and Q. Li, *Chin. J. Catal.*, 2020, **41**, 200–208.
197 F. Qiu, W. Li, F. Wang, H. Li, X. Liu and J. Sun, *J. Colloid Interface Sci.*, 2017, **493**, 1–9.
198 X. Chen, Z. Han, Z. Lu, T. Qu, C. Liang, Y. Wang, B. Zhang, X. Han and P. Xu, *Sustainable Energy Fuels*, 2023, **7**, 1311–1321.
199 W. Ren, J. Yang, W. Chen, J. Zhang, Y. Sun, Y. Zheng, H. Zhao and B. Liang, *Mater. Res. Bull.*, 2022, **153**, 111884.
200 C. Zhang, J. Ma, H. Zhu, H. Ding, H. Wu, K. Zhang, X. L. Zhao, X. Wang and C. Cheng, *J. Alloys Compd.*, 2023, **960**, 170932.
201 Q. Li, S. He, L. Wang, J. Song, J. Wang, C. Shao, Z. Tian and Y. Liu, *CrystEngComm*, 2023, **25**, 2882–2891.